1 **High-precision atmospheric oxygen measurement comparisons between a newly built**

2 **CRDS analyzer and existing measurement techniques**

4 Tesfaye A. Berhanu[1,2], John Hoffnagle[2], Chris Rella[2], David Kimhak[2], Peter Nyfeler[1], Markus

5 Leuenberger[1]

6 [1]*Climate and Environmental Physics, Physics Institute and Oeschger Centre for Climate Change Research,*

7 *University of Bern, Bern, Switzerland*

8 [2]*Picarro Inc., 3105 Patrick Henry Drive, Santa Clara, CA, USA*

10 **Abstract**

11 Carbon dioxide and oxygen are tightly coupled in land-biospheres CO_2 - O_2 exchange

12 processes, while they are not coupled in oceanic exchange. For this reason, atmospheric

13 oxygen measurements can be used to constrain the global carbon cycle, especially oceanic

14 uptake. However, accurately quantifying the small (~1-100 ppm) variations in O_2 is

15 analytically challenging due to the very large atmospheric background which constitutes

16 about 20.9 % (~209500 ppm) of atmospheric air. Here we present detailed description of the

17 analyzer and its operating principles as well as comprehensive laboratory and field studies for

18 a newly developed high-precision oxygen mixing ratio and isotopic composition analyzer

19 (Picarro G-2207) that is based on cavity ring-down spectroscopy (CRDS). From the

20 laboratory tests, we have calculated a short-term precision (standard error of one-minute O_2

21 mixing ratio measurements) of < 1 ppm for this analyzer based on measurements of eight

22 standard gases analyzed for two hours consecutively. In contrast to the currently existing

23 techniques, the instrument has an excellent long-term stability and therefore a calibration

24 every 12 hours is sufficient to get an overall uncertainty of < 5 ppm. Measurements of

ambient air were also conducted at the High-Altitude Research Station, Jungfraujoch and the Beromünster tall tower in Switzerland. At both sites, we observed opposing and diurnally varying CO_2 and O_2 profiles due to different processes such as combustion, photosynthesis and respiration. Based on the combined measurements at Beromünster tower, we determined height dependent $O_2:CO_2$ oxidation ratios varying between -0.98 to -1.60 , which increase with the height of the tower inlet, possibly due to different source contribution such as natural gas combustion with high oxidation ratio and biological processes which are at the lower end.

1. Introduction

Atmospheric oxygen comprises about 20.9 % of the global atmosphere and in the past decade its concentration decreased at a rate of ~ 20 per meg yr^{-1} (Keeling and Manning, 2014) mainly associated with the increase in fossil fuel combustion. Note that the variations in atmospheric O_2 is expressed in units of per meg due to its small variations with respect to a large background and to account for dilution effects from CO_2 or any other gas of relevant amount change which is expressed as:

$$\delta \left(\frac{O_2}{N_2}\right)(per\ meg) = \left(\frac{(\frac{O_2}{N_2})sample}{(\frac{O_2}{N_2})reference} - 1\right).10^6 \qquad (1)$$

In contrast, the global average atmospheric CO_2 mixing ratio increased to 405.0 ppm averaged over 2017 since its preindustrial value of 280 ppm (Le Quéré et al., 2017). As the variability of atmospheric oxygen is directly linked to the carbon cycle, both its short and long-term observations can be used to better constrain the carbon cycle. For example, since first suggested by Keeling and Shertz (1992) the long-term trends derived from concurrent measurements of atmospheric CO_2 and O_2 have been widely used to quantify the partitioning of atmospheric CO_2 between the land-biosphere and oceanic sinks (Battle et al., 2000; Goto et

al., 2017; Manning and Keeling, 2006; Valentino et al., 2008). This method hinges on the linear coupling between CO_2 and O_2 with an oxidation ratio (OR defined as the stoichiometric ratio of exchange during various process such as photosynthesis and respiration) of 1.1 for the terrestrial biosphere photosynthesis-respiration processes (α_b) and 1.4 for fossil fuel combustion (α_f) while they are decoupled for oceanic processes. Meanwhile, the short-term variability in atmospheric oxygen can be used to estimate marine biological productivity and air-sea gas exchange (Keeling et al., 1998; Nevison et al., 2012). However, the accuracy of these estimates is primarily linked to the accuracy and precision of atmospheric O_2 measurements and the assumed ORs for the different processes which are highly variable in contrast to atmospheric CO_2 that can be well measured within the precision guidelines set by the Global Atmospheric Watch (GAW) (± 0.1 ppm for the northern hemisphere).

Currently there are several techniques mostly custom built that can measure atmospheric O_2 variations as oxygen concentration based on interferometric, paramagnetic, UV absorption and fuel cell technology (Keeling, 1988a; Manning et al., 1999; Stephens et al., 2007) or as O_2/N_2 ratios to account for the large background effect using gas chromatography with thermal conductivity detector (GC-TCD) or gas chromatography coupled to mass spectrometry (GC-MS) (Bender et al., 1994; Tohjima, 2000). Despite the fact that these techniques have been used for more than two decades, accurate quantification of atmospheric oxygen variability remains challenging primarily because the small ppm-level atmospheric oxygen signal rides on a ~ 210,000 ppm background, which places stringent requirements on the precision and drift of the analysis methods especially for continuous monitoring(Note that the GAW recommendation for the measurement precision of O_2/N_2 is 2 per meg). The techniques listed above struggle to routinely achieve the necessary performance for various reasons, including i) instability over time that requires frequent measurement

72 interruption for calibration, ii) measurement bias with ambient and sample temperature and/or

73 pressure, and/or iii) systematic errors in the measurement due to other atmospheric species.

74 Further, some techniques require the use of consumables and rely on high vacuum, which

75 complicates field deployment.

76   In this manuscript we describe a new high precision oxygen concentration and isotopic

77 composition analyzer by Picarro Inc., Santa Clara, USA (G-2207) based on CRDS

78 technology. Here, we will introduce the analyzer design principles in details, describe the

79 unique features of the analyzer and evaluate its performance based on various independent

80 laboratory and field tests by comparing it with currently existing techniques. Then, we will

81 present and interpret our observations based on field measurements. Finally, we will conclude

82 its overall performance and provide recommendations and possible improvements.

83 **2. Analyzer design principles**

84   The analyzer described here is derived from the Picarro G2000 series of CRDS

85 analyzers. The basic elements have been described elsewhere (Crosson, 2008; Martin et al.,

86 2016; Steig et al., 2014): briefly, the instrument is built around a high-finesse, traveling-wave

87 optical cavity, which is coupled to either of two single-frequency Distributed Feedback-

88 stabilized semiconductor lasers. One cavity mirror is mounted on a piezoelectric translator

89 (PZT) to allow fine tuning of the cavity resonance frequencies. A semiconductor optical

90 amplifier between the laser sources and the cavity boosts the laser power and serves as a fast-

91 optical switch. The cavity body is constructed of invar and enclosed in a temperature

92 stabilized box (T = 45° C, stabilized to approximately 0.01 °C) for dimensional and

93 spectroscopic stability. A vacuum pump pulls the gas to be sampled through the cavity and a

94 proportional valve between the cavity and the pump maintains the sample pressure in the

95 cavity at a value of 340 hPa, with variations on the order of 1 Pa. The instrument has a

wavelength monitor, based upon measurements of interference fringes from a solid etalon, which is used to control the laser wavelength by adjusting the laser temperature and current. A high-speed photodiode monitors the optical power emerging from the cavity. The instrument's data acquisition system sweeps the laser frequency over the spectral feature to be measured, modulates the laser output to initiate ring-downs, and fits the ring-down signal to an exponential function to generate a spectrogram of optical loss versus laser frequency. For this instrument the empty cavity ring-down time constant is about 39 μs. Subsequent program modules compare the measured loss spectrum to a spectral model, using non-linear least-squares fitting (Press et al., 1986) to find the best-fit model parameters and thereby obtain a quantitative measure of the absorption due to the target molecule, and finally apply a calibration factor to the optical absorption to deduce the molecular concentration. When operating in its normal gas analysis mode, the instrument acquires about 200-300 ring-downs per second and achieves a noise equivalent absorption of typically about 10^{-11} cm^{-1} Hz$^{-1/2}$, with some variation between instruments.

The primary goal when designing this analyzer was to measure the molecular oxygen concentration with few-per-meg level precision and stability. In this context operational stability is as important as signal-to-noise. Our experience has been that the most stable operation of the analyzer is achieved when the optical phase length of the cavity is held as nearly constant as possible. In this case the free spectral range (FSR, 0.0206 cm^{-1}) of the temperature stabilized, invar ring-down cavity provides a better optical frequency standard than the etalon-based wavelength monitor, which in turn allows more consistent measurements of absorption line width and integrated absorption line intensity (Steig et al., 2014). For a small, field-deployable instrument, it is not practical to stabilize the absolute frequencies of the cavity modes to an optical frequency standard (Hodges et al., 2004) but the

120 oxygen lines themselves, under conditions of constant temperature and pressure, provide an

121 adequate frequency reference. The oxygen spectrum was also used to calibrate the FSR, by

122 comparing a wide (approximately 10 cm^{-1}) FSR-spaced spectrum with the Hitran database

123 (Rothman et al., 2013).

124   To determine molecular oxygen concentration, the analyzer measures absorption of the

125 Q13Q13 component of the $a^1\Delta_g \leftarrow X^3\Sigma^-_g$ band, at a frequency of 7878.805547 cm^{-1},

126 according to the latest edition of Hitran (Gordon et al., 2017). This is one of the strongest

127 near-infrared lines of oxygen, well separated from other oxygen lines, and reasonably free of

128 spectral interference from water, carbon dioxide, methane, and other constituents of clean air.

129 The spectral model for this line was developed using reference spectra of clean, dry, synthetic

130 air that were acquired with the same hardware as in the field-deployable analyzer, but with

131 special-purpose software that allows it to operate as a more general spectrometer.

132   Recently, considerable work has been done to advance the understanding of spectral

133 line shapes and to define functional representations that better describe the processes that

134 determine spectral line shapes than does the Voigt model (Hartmann et al., 2008; Tennyson et

135 al., 2014, Tran et al., 2019). Line shape studies have been published for the 1.27 μm band of

136 O$_2$ (Fleisher et al., 2015; Lamouroux et al., 2014), though not to our knowledge for the Q

137 branch. The apparatus used here is not capable of spectroscopic studies of comparable

138 precision; the absolute temperature and pressure monitoring and especially the frequency

139 metrology are far too crude for that purpose. Our goal is merely to define a simple model of

140 the Q13Q13 line that is adequate for least-squares retrievals of the O$_2$ absorption under the

141 limited range of conditions (stabilized temperature and pressure) that the operational analyzer

142 experiences in the field. The CRDS analyzers use the Galatry function (Varghese and Hanson,

143 1984), which is distinctly better than the Voigt and still easily and quickly evaluated for line

144 shape modeling. Ultimately, the usefulness of the spectral model is to be evaluated by the

145 precision and stability of the O_2 measurements when compared with established techniques.

146 Ultimately, the usefulness of the spectral model is to be evaluated by the precision and stability of

147 the O_2 measurements when compared with established techniques.For spectral model

148 development, this spectrometer has the drawback that the cavity FSR, is too large to reveal

149 much detail of the absorption line shape, even with the simplifying assumption of a Galatry

150 line shape. We therefore acquired a set of four interleaved spectra, with the PZT-actuated

151 mirror moved to offset the cavity modes of the individual FSR-spaced spectra by one-fourth

152 of an FSR. The precise offsets were determined from fits to the strong and well-isolated O_2

153 lines in the spectra. From the consistency of the fitted line centers, we estimate that the

154 positioning of the interleaved spectra was accurate to approximately 10 MHz. The spectrum

155 of the Q13Q13 line acquired in this manner is shown in Figure 1, together with the best-fit

156 Galatry function. It stands out that the residuals are largely odd in detuning from the line

157 center: this shows the limitations of the Galatry model in this case, since the Galatry function

158 is purely even about the line center. The shape of the absorption line in this model is specified

159 by two dimensionless parameters: the collisional broadening parameter

160 $y = \gamma/\sigma_D$ (2)

161 and the collisional narrowing parameter

162 $z = \beta/\sigma_D$ (3)

163 where γ is the frequency of broadening transitions, β is the velocity change collision rate, and

164 σ_D is the 1/e Doppler half-width of the transition, given by

165 $\sigma_D = \nu_0(2k_BT/Mc^2)^{1/2}$ (4)

166 where ν_0 is the transition frequency, k_B is Boltzmann's constant (J. K^{-1}), T is the sample

167 temperature (K), M is the molecular mass (amu), and c is the speed of light (m/s). Figure 2

168   shows the values of y and z obtained from spectra acquired in the same way as Figure 1, as a

169   function of cavity pressure. The values depend linearly on pressure, as expected from the

170   Galatry model, but the unconstrained linear fits do not go precisely through the origin. It is

171   not clear whether this represents a breakdown of the Galatry model or simply reflects the

172   limited quality of the data set. The slope of y can be converted to an air-broadened collisional

173   width $\gamma_{air} = 0.0442$ cm^{-1}/atm, which agrees with the Hitran value of 0.0460 cm^{-1}/atm (Gordon

174   et al., 2016) to within the uncertainty estimate stated by Hitran (uncertainty code 4 for γ_{air}

175   corresponding to 10% --20% relative uncertainty). The slope of z can be interpreted in terms of

176   the optical diffusion coefficient (Fleisher et al., 2015), yielding $D = 0.285$ cm^2 s^{-1}, compared

177   to the literature value of 0.233 cm^2 s^{-1} for O_2 in air at 45 °C (Marrero and Mason, 1972).

178   Although the anticipated use of the analyzer is for ambient air samples having a very small

179   range of O_2 concentrations, we did investigate the variation of the line shape in binary

180   mixtures of O_2 and N_2 shown in Figure 3. The error bars are taken from the output of the

181   Levenberg-Marquardt fitting routine (Press et al., 1992). The dependence of the collisional

182   broadening parameter z on O_2 mole fraction was considered too small to be significant, but

183   the variation in y was used in the subsequent analysis of the air samples. Note that Wójtewicz

184   et al. (Wójtewicz et al., 2014) also found collisional broadening coefficients for nitrogen to be

185   slightly larger than for oxygen in measurements of one O_2 line in the B-band.

186   The primary goal in designing the analyzer was to achieve high enough precision to

187   make meaningful measurements of O_2 in clean atmospheric samples. Although the current

188   best practice for such high-precision measurements is to work with dried samples, we decided

189   to include high precision measurements of water vapor. There were two reasons for this

190   decision: one is to serve as a monitor for residual water vapor, which is difficult to remove

191 completely from the ring-down cavity and associated sample handling hardware, and the

192 second and more ambitious reason was to see how well the effect of water vapor could be

193 corrected for measurements of undried ambient air. While it was considered unlikely that

194 measurements of undried air could compete in accuracy with those of dried air, it might be

195 possible to correct for water vapor well enough to enable useful measurements in some

196 circumstances without the expense and inconvenience of drying the sample. For this purpose,

197 a second laser was added, which probes the $7_{1,6} \rightarrow 8_{4,5}$ component of the $2v_3$ band of water

198 vapor, at a frequency of 7816.75210 cm^{-1} (Gordon et al., 2017). The Galatry model was used

199 to fit spectra of synthetic air humidified to various levels of water vapor concentration. These

200 fits also included two other nearby, very weak water lines, with intensities less than 1% of the

201 strong transition, in order that their absorption should not perturb the line shape of the main

202 transition. Results for the shape of the 7816.75210 cm^{-1} line are shown in Figure 4. At the

203 level that we can measure, only the y-parameter has a meaningful variation with water

204 concentration. From the linear fit one obtains a pressure broadening coefficient for air, γ_{air} =

205 0.0752 cm^{-1}/atm, in reasonable agreement with the Hitran value γ_{air} = 0.0787 cm^{-1}/atm

206 (Gordon et al., 2017), and a self-broadening coefficient γ_{self} = 0.413 cm^{-1}/atm, to be compared

207 with the Hitran value γ_{self} = 0.366 cm^{-1}/atm. Since the uncertainty estimate for the Hitran

208 values is 10 % to 20 %, this level of agreement seems reasonable.

209   We also looked at absorption from water near the Q13Q13 absorption line of O_2.

210 These spectra were measured in a background of pure nitrogen to reveal the very weak lines

211 interfering with the O_2 measurement. Without the strong O_2 lines, it was impossible to

212 interleave FSR-spaced spectra, so in this case the frequency axis comes from the analyzer's

213 wavelength monitor. The upper panel of Figure 5 shows the spectrum of saturated water vapor

214 in nitrogen, together with a fit to a Voigt model of the molecular lines. The measurement was

215   made at a pressure of 340 hPa and temperature of 45° C. The main features are the Q13Q13 line

216   from trace contamination of oxygen in the sample and several lines that arise from normal water

217   ($^1H_2^{16}O$, AFGL abbreviation 161) and deuterated water ($^1H^2H^{16}O$, AFGL abbreviation 162, also

218   abbreviated HDO). The lower panel of Figure 5 shows the lines tabulated in Hitran.

219   Immediately after the data in Figure 5 were acquired, measurements were also made at

220   7816.85210 cm^{-1}, to establish the relationship between the absorption strengths in the two

221   spectral regions. The relative intensities of the 161 and 162 lines change with variations in the

222   isotopic composition of the water, but fortunately the direct interference with the oxygen Q13Q13

223   lines comes entirely from the 161 isotopologue, with the strongest 162 line being separated by

224   approximately 8 line widths (FWHM) from the Q13Q13 line.   Hitran simulations for molecules

225   other than water that are expected to be present in clean, ambient air indicate that direct

226   interference with the Q13Q13 line should be negligible at the level of precision considered

227   here. In the case of CO_2, the dilution of oxygen due to 400 ppm of CO_2 is significant, and

228   larger than any direct spectral interference.

229   Finally, we investigated the influence of water vapor on the shape of the O_2 Q13Q13

230   line. Switching between the two lasers sources, we acquired FSR-spaced spectra of

231   humidified synthetic air, alternately covering the 7817 cm^{-1} and 7878 cm^{-1} regions. Individual

232   spectra were acquired in less than 2 s, so changes in water vapor concentration between

233   spectra were small. These spectra, with frequency resolution of 0.0206 cm^{-1}, were analyzed by

234   nonlinear least-squares fitting with the following spectral models: the 7817 cm^{-1} spectra were

235   modeled as the sum of an empty-cavity baseline having an adjustable offset level and slope

236   and three water peaks and the two weak perturbing peaks. The molecular absorption of the

237   main peak was expressed as an adjustable amplitude, A_w, multiplying a dimensionless, area-

238   normalized Galatry function (Varghese and Hanson, 1984).   The weak perturbers were

239   modeled by Voigt profiles with amplitudes and line widths that constrained to be in fixed

240   ratios to the strong line, and therefore added no new degrees of freedom to the fitting

241   procedure. Since the amplitude A_w multiplies an area-normalized shape function, it is

242   essentially equivalent to the area of the absorption line, to the extent that the Galatry model

243   provides a valid description of the line shape. The Doppler width of the Galatry function was

244   fixed based on the measured cell temperature, the y-parameter was allowed to vary, and the z-

245   parameter was constrained to be proportional to y, based on measurements summarized in

246   Figure 2. In addition, the center frequency of the Galatry function was adjusted to match the

247   data set, giving a total of five free parameters for this fit. The 7878 cm^{-1} spectra were modeled

248   with an adjustable baseline offset and slope and molecular absorption amplitude, A_{O2},

249   describing the Q13Q13 O_2 line. Here, too, the y-parameter and centration of the O_2 lines were

250   allowed to adjust, and the z-parameter was constrained to be proportional to y. The weak

251   water lines interfering with oxygen absorption were included in the model, but with no

252   additional free parameters, rather the amplitudes were preset based on the measured water

253   absorption at 7817 cm^{-1} and the previously determined amplitude relationships between the

254   water lines. This procedure does not account for variations in HDO abundance, which may introduce

255   some systematic error into the water vapor correction for samples of unusual isotopic composition,

256   but it should accurately model the most important lines that interfere with the oxygen

257   measurement. Collisional broadening of the Q13Q13 O_2 line by water vapor is shown in

258   Figure 6. From the linear fit one obtains a coefficient for collisional broadening of the

259   Q13Q13 line by water vapor of γ_{water} = 0.0442 cm^{-1}/atm. We are not aware of previous

260   measurements of this quantity.

261   The alternating measurements at 7817 cm^{-1} and 7878 cm^{-1} also calibrated the

262   relationship between water mole fraction and the absorption at 7817 cm^{-1}, using a dilution

263 analysis described by Filges et al. (Filges et al., 2018), who showed that the results obtained

264 this way agree well with water vapor fractions measured with a conventional hygrometer.

265 Figure 7 shows the measured amplitudes of the water and oxygen lines for samples of variable

266 humidity. Since the air came from a tank of constant composition, the oxygen concentration

267 changes due to dilution of oxygen when water is added. Assuming that this is the sole cause

268 of the change in measured absorption, since the line shapes were being constantly adjusted to

269 account for changes in collisional broadening, it is straightforward to deduce the relation

270 between the water fraction and the absorption amplitude. This calibration was used to

271 generate the water fraction axes in Figures 4 and 6. We note that we did not take particular

272 care to control or measure the quantity of dissolved gases, especially oxygen and carbon

273 dioxide, in the water used for this experiment. While these gases would not significantly

274 affect the water calibration, they may affect the water vapor correction of the oxygen

275 measurement at the ppm level. More work needs to be done to investigate the water vapor

276 correction of the oxygen measurement.

277 The observations described above were used to design a method to measure oxygen

278 concentration in ambient air. Gas from the inlet to the analyzer is drawn through the cavity at

279 a rate of about 100 sccm (standard cubic centimeter per minute) and the conditions in the

280 cavity are held stable at 340 hPa and 45° C. In its analysis mode the analyzer alternately

281 measures ring-downs in the 7817 cm^{-1} and 7878 cm^{-1} regions. At 7878 cm^{-1} measurements are

282 made at 11 different frequencies, spaced by one FSR of the cavity and centered at the peak of

283 the Q13Q13 line. Multiple ring-down measurements are made to improve the precision of the

284 loss determination, with a total of 305 ring-downs allocated to one spectrum. In the 7817 cm^{-1}

285 region measurements are also made at 11 distinct frequencies at FSR spacings. Only 35 ring-

286 downs are allocated to this spectral region, since the measurement of O_2 is much more

287 important than water vapor. The data sets are analysed using a Levenberg-Marquardt fitting

288 routine, which adjusts five free parameters in each region to find the best agreement to a

289 spectral model based on Galatry line shapes, as described above. One of the outputs of the

290 7878 cm^{-1} fit is the frequency offset of the FSR grid from the center of the Q13Q13 line. This

291 information is used to adjust the position of the PZT actuated mirror to keep the

292 measurements centered on the line, effectively stabilizing the optical path length of the cavity

293 to the frequency of the O_2 line. The reported water fraction is obtained by multiplying the

294 fitted amplitude of the water line by a calibration constant derived from the dilution

295 experiment as explained above. For the O_2 fraction a slightly more complicated procedure is

296 followed. It was observed that the least-squares fitting of the data gives highly correlated

297 results for the amplitude of the absorption line and the line width parameter y. The correlation

298 may be due in part to the fitting procedure itself (Press et al., 1992) and it may also have a

299 contribution from pressure variations that the pressure sensor is unable to detect. The ratio

300 A_{O2}/y can be determined from the fit much more precisely than A_{O2} alone and so gives a more

301 sensitive measurement of molecular absorption. It also has the advantage of being

302 independent of sample pressure, to the extent that the Galatry model applies (Figure 2).

303 However, using the ratio A_{O2}/y as a metric for absorption adds more complications if

304 measurements are to be made over a range of O_2 and water concentrations, because the O_2/ N_2

305 ratio and water concentration affect the line width independently of pressure and O_2

306 concentration alone. To minimize systematic errors due to these broadening effects, we define

307 a nominal y-parameter based on the measured amplitudes of the O_2 and water lines and the

308 line broadening dependences shown in Figures 3 and 4. The measured ratio A_{O2}/y is

309 normalized by the nominal y to obtain a quantity that is ideally independent of pressure and

310 water concentration, and this is the quantity that is multiplied by a calibration constant to give

311 the reported O_2 fraction. In addition, a dry mole fraction is reported for O_2, defined as the

312 directly measured mole fraction corrected for water dilution.

313   The main goal in developing this instrument was to make high precision

314 measurements of O_2 mole fraction, based on absorption by the dominant $^{16}O_2$ isotopologue.

315 The absorption lines of the rarer isotopologues are also present nearby, so a mode of operation

316 was included in which one laser is scanned over neighboring lines of $^{16}O_2$ and $^{16}O^{18}O$ and the

317 ratio of amplitudes is used to derive an isotopic ratio, reported in the usual delta notation. In

318 this case the operating pressure was reduced to 160 hPa to improve the resolution of the

319 nearby lines. The lines measured were the Q3Q3 line of $^{16}O_2$, at 7882.18670 cm^{-1}, and the

320 Q9Q9 line of $^{16}O^{18}O$, at 7882.050155 cm^{-1}. The measurement procedure is very much like

321 that for the O_2 fraction measurement, so it will not be described in detail, only the main

322 differences will be noted. One is that in determining an isotopic ratio there is no advantage to

323 be obtained from normalizing absorption amplitudes to line widths, instead we simply take

324 the ratio of amplitudes to compute delta. Although the Q9Q9 line and its neighbor Q8Q8 are

325 the strongest ones in this band, absorption by $^{16}O^{18}O$ is still very weak, only about 5x10^{-9} cm^{-1}

326 at the line center under the conditions we used. Consequently, the signal-to-noise that can be

327 achieved with this analyzer is not adequate to determine both the amplitude and the width of

328 the $^{16}O^{18}O$ line with useful precision, so in the fitting step the y-parameter of the $^{16}O^{18}O$ line

329 is constrained to be a constant factor times the fitted y-parameter for the $^{16}O_2$ line.

330 Additionally, because of the weakness of the rare isotopologue absorption, the majority of

331 ring-downs in each spectrum is devoted to measuring $^{16}O^{18}O$ i.e. 232 ring-downs in each

332 spectrum versus only 40 for $^{16}O_2$. This implies that the mole fraction measurement in the

333 isotopic mode is much less precise than when the analyzer measures the Q13Q13 line alone.

334 **3. Results and Discussions**

3.1. Laboratory tests at Picarro, Santa Clara

3.1.1. Temperature and pressure sensitivity

One set of tests was done to determine how well the goal was met of minimizing the susceptibility of the concentration measurements to uncontrolled noise or drift of the sample temperature and pressure. For these tests the analyzer sampled dry synthetic air from a tank and the temperature and pressure setpoints of the cavity were adjusted upward and downward from the nominal values, to obtain an estimate of the differential response. We express the sensitivity to experimental conditions in relative form, that is the derivative with respect to temperature or pressure divided by the signal under nominal conditions.

From these experiments, we determined a temperature sensitivity of -2.1×10^{-4} K^{-1} and a pressure sensitivity of $+9.8 \times 10^{-6}$ hPa^{-1}. The temperature sensitivity is somewhat larger than expected based on a calculation using Hitran data to estimate the temperature dependences of all the quantities that go into the measured absorption of the Q13Q13 line. The pressure sensitivity is strikingly small, indicating a good cancelation of the pressure dependence of absorption amplitude and line width. Both temperature and pressure sensitivities are small enough to have a negligible effect on short-term precision of measurements made with the stabilized ring-down cavity, though long-term drifts in the sensors are always a matter of concern.

3.1.2. Measurement precision and Drift

Measurement precision was evaluated by analyzing synthetic air containing nominal atmospheric concentrations of CO_2 and CH_4 from an aluminum Luxfer cylinder over a period of several days. The tank, oriented horizontally and thermally insolated (though not controlled), was connected directly to the instrument (S/N TADS2001) with a 2-stage regulator and stainless-steel tubing and reducing the flow with an additional orifice to about

359 55 sccm. For the isotopic mode of operation, the precision of the measurement was also tested

360 by making repeated measurements from a tank of clean, dry synthetic air.

361   Figure 8 shows the time series of the precision test data, displaying the reported

362 oxygen concentration, the height of the oxygen absorption peak, the width of the oxygen

363 absorption peak and the ambient temperature. The residual error of the analyzer, although

364 small, is nevertheless significant given the stringent targets set forth by the WMO-GAW

365 program. Possible sources of error include: temperature drifts due to sensor drift or gradients;

366 pressure errors due to sensor drift; optical artifacts such as parasitic reflections, higher order

367 cavity mode excitation, and/or loss nonlinearity that can distort the reported oxygen spectrum.

368 More work is required to identify and eliminate these small drifts.

369   The Allan standard deviation of the reported O_2 fraction is shown in Figure 9. The

370 ordinate on this plot is the square root of the Allan variance of reported mole fraction, so 1

371 ppm in these units corresponds to about 5 per meg in the ratio of O_2/N_2. The precision of

372 averaged measurements improves as $\tau^{-1/2}$ for approximately 5000 s and reaches 1 ppm in less

373 than 10 minutes and remains below 1 ppm for time scales on the order of about 1 hour.

374   Figure 10 shows the precision of $\delta(^{18}O)$ (uncalibrated) derived from the ratio of lines

375 measured at 7882 cm^{-1}. Because of the weak signal from the $^{16}O^{18}O$ line, it is necessary to

376 average for more than 20 seconds or more to achieve 1‰ precision on the isotopic ratio. As

377 for the concentration measurement, averaging improves the measurement precision for times

378 scale up to about 1 hour.

3.2. Laboratory measurements at the University of Bern

3.2.1. Measurements of standard gases

381   The performance of the instrument was tested by analyzing eight standard gases with

382 precisely known CO_2 and O_2 compositions (Table 1) using the CRDS analyzer and comparing

383 it to parallel measurements with a paramagnetic oxygen sensor (PM1155 oxygen transducer,

384 Servomex Ltd, UK) embedded to a commercially available Oxzilla fuel cell oxygen analyzer

385 (OXZILLA II, Sable Systems International, USA) (Sturm et al., 2006) as well as with an

386 isotope ratio mass spectrometer (IRMS, Finnigan Delta^{Plus}XP). The design of the

387 measurement set-up is shown in Figure 11. Standard gases were directly connected to the

388 pressure controlling unit, and a multi-port valve (V2) was used to select among the standard

389 gases. The flow from each cylinder was adjusted to about 120 ml min^{-1} which was eventually

390 directed to a selection valve (V1), allowing switching between ambient air and standard gases.

391 Flow towards and out of the Oxzilla was controlled by the pressure controlling unit. The O_2

392 mixing ratio of this incoming gas was first measured on the Paramagnetic O_2 sensor and then

393 directed towards a non-dispersive infrared analyzer (NDIR) (Li-7000, LICOR, USA) for

394 measuring CO_2 and H_2O. The outflow from this analyzer (100 ml min^{-1}) returns to the

395 pressure controlling unit and was eventually divided between the CRDS analyzer (which uses

396 about 75-80 ml min^{-1}) and the IRMS (~ 20 ml min^{-1}) via a Tee-junction. Each cylinder was

397 measured for two hours in each system controlled by a Lab VIEW program.

398   In priori, we investigated the influence of this Tee-junction, which splits the gas flow

399 between the CRDS and the IRMS, on the measured O_2 values. Manning (2001) showed that

400 the fractionation of O_2 in the presence of a Tee-Junction is strongly dependent on the splitting

401 ratios as well as temperature and pressure gradients. Hence, we measured and compared the

402 O_2 mixing ratios of two standard gases (CA07045 and CA060943) in two cases: i) in the

403 presence of a Tee-junction with different CRDS to IRMS splitting ratios and ii) without a

404 Tee-junction so that all gas flow is directed towards the CRDS analyzer. The splitting ratios in

405 these test experiments vary from 1:1 to 1:100, and reversed to change the major flow direction

406 either to the CRDS or the IRMS. Note that the experimental condition in this manuscript is

407 with a 4:1 splitting ratio (i.e. ~ 80 ml min^{-1} towards the CRDS analyzer and ~ 20 ml min^{-1}

408 towards the IRMS).

409 In the cases of the smaller splitting ratios (1:1, 1:4 and 4:1), which are relevant for the

410 results presented in this study, only minor differences in the measured O_2 mixing ratios were

411 observed when compared to case ii (i.e. without a Tee-junction). For these two cylinders

412 measured, the average differences in these cases were about 0.5 ppm, calculated as the mean

413 of the differences in the raw O_2 measurements of the last 60 seconds. The negligible

414 fractionation can indeed be the result of smaller splitting ratios while strong influence is

415 usually expected in case of larger splitting ratios (Stephens et al., 2007). For higher splitting

416 ratios, the result seems inconclusive without any dependence on the ratios due to the strong

417 decline in the cylinder temperature (specifically at the pressure gauge) caused by higher flow

418 to achieve the higher splitting ratios (as high as 1:100). Hence, these tests need to be

419 conducted in a temperature controlled condition and the results could not be discussed in this

420 manuscript.

421 Figure 12 shows the standard gas measurements for the seven cylinders with known

422 CO_2 and O_2 mixing ratios (Table 1) using both the CRDS and the Paramagnetic analyzers.

423 Standard eight, which has too high O_2, is not shown in the figure as the figure is zoomed-in to

424 better illustrate the change in O_2 for the remaining cylinders. While the first five cylinders

425 contain O_2 and CO_2 fractions comparable to ambient air values, standards 6 & 8 had either

426 very low and very high O_2, respectively. In addition, standard 6 and 7 have very low and very

427 high CO_2 mixing ratios. Note that due to its very high CO_2 content (~ 2700 ppm), standard 7

428 was not measured on the IRMS and hence the O_2 mixing ratios are unknown. The measured

429 mixing ratios for the six standard gases between the two systems are in very good agreement

430 while cylinder 7 showed an opposing signal for the two analyzers compared to standard 6

431   (Figure 12). While the Paramagnetic analyzer showed a higher O_2 mixing ratio, the values

432   from the CRDS analyzer are lower in O_2. This can be associated with the very high CO_2

433   mixing ratio in standard 7, which leads to a strong dilution effect in the CRDS analyzer as it

434   does not include any correction function for dilution effect from CO_2. However, such high

435   CO_2 mixing ratios may not be that important for most atmospheric research. Yet, it should be

436   considered to include a parallel CO_2 mixing ratios measurement to the instrument as it will

437   further improve the accuracy. This would be especially important for biological or

438   physiological studies where a wide range of CO_2 and O_2 concentrations must be expected.

439   The measurement precision of the CRDS analyzer was calculated as the standard error

440   of the mean i.e. the standard deviation (1-σ) of the last 1-minute raw measurements divided

441   by the square root of the number of measurements (n = 60), and for all these cylinders the

442   values are usually between 0.5 ppm to 0.7 ppm. For parallel measurements of these cylinders

443   using a Paramagnetic analyzer, we obtained a precision of about 1 ppm, calculated exactly the

444   same way.

445   We also made a correlation plot to see which of the two instruments are in better

446   agreement with the assigned values based on IRMS measurements for the individual

447   cylinders. While similar correlation coefficients were observed for both analyzers, different

448   slopes were calculated (Fig. A.1). This is due to the fact that the IRMS measures the O_2 to N_2

449   ratio ($\delta(O_2/N_2)$) in per meg, while the CRDS and the Paramagnetic analyzers provide non-

450   calibrated O_2 mixing ratios in units of ppm and per meg, respectively. If we exclude the two

451   standard gases with the highest and lowest O_2 mixing ratios (standards 7 and 8) that are

452   subjected to strong dilution effects, both the slope and the r^2 values decrease from those

453   shown in Figure A.1. But this decrease is larger in the case of the Paramagnetic

454   measurements, implying a slightly better linearity of the CRDS analyzer.

3.2.2. Measurements of ambient air

Ambient air measurements were conducted from the roof top of our laboratory at the University of Bern to evaluate the analyzer's performance under atmospheric variability. Ambient air was continuously aspirated from the inlet at the roof of the building at a flow rate of ~ 250 ml min^{-1} which is then dried using a cooling trap kept at -90 °C towards the switching valve (V1) and measured in similar way to the standard gases as explained above. The measurement values obtained here were compared with the parallel measurements by the Paramagnetic sensor to test the instruments stability and accuracy.

Figures 13 panels a &b show the 1-minute average ambient air measurements from the rooftop inlet by the Paramagnetic and the CRDS analyzers at the beginning of the testing period including standard gases measured every 12-hour. While the Paramagnetic analyzer seems to be stable, the CRDS analyzer showed a strong drift for an extended period. This can be due to unstable conditions in the CRDS measurement system as it started operating right after it was unpacked. Hence, we looked into temperature inside the instrument chassis and pressure records, which were stable within the manufacturer's recommended range during this period. As the CRDS analyzer incorporates a water correction function, interference from this species should be well accounted. Even comparing the analyzer's parallel water measurements to water measurements by the NDIR system such a drift was not observed. It should be noted that the two internal standard gases which were less frequently measured (every 12 hours) during this period were also drifting in similar pattern. This implies that the drift is associated with the analyzer. Interestingly, we observed that the two cylinders follow exactly the same drift pattern that can be modeled using a polynomial function which can then be used to correct for the observed drift in the ambient air measurements. After applying a polynomial drift correction, we were able to fully account for the observed drift. However, the

479 manufacturer decided to further investigate possible causes of this drift. After further

480 improvements, we obtained the first commercial analyzer in September 2017 and repeated the

481 above tests (Figure 13 c &d). No such drift was observed any more in the standard gases or in

482 ambient air measurements.

483 A possible hypothesis for the cause of the drift can be an optical amplifier in the first system

484 and not anymore included in the design of the product which produced a significant amount of

485 broadband light that could fill the cavity (albeit with a low coupling coefficient), and would

486 ring down with a different (and generally much faster) time constant that the baseline loss of

487 the cavity. However, the ringdown time on the peak of the oxygen line is just 10

488 microseconds, such that the broadband light might have distorted the single exponential decay

489 of the central laser frequency, leading to the observed drift in the oxygen signal. However,

490 we were not able to confirm this hypothesis.

491 3.2.3. Water correction test

492 Measurements of oxygen are reported as both wet ($O_{2, raw}$) and dry ($O_{2, dry}$) mole

493 fractions by the CRDS analyzer as it also measures water vapor in parallel at its water

494 absorption line (7817 cm^{-1}), and corrects for the dilution effect based on an inbuilt numerical

495 function:

496
$$O_{2,dry} = \frac{O_{2,raw}}{1 - f_{H_2O}} \qquad (5)$$

497 where f_{H2O} is the measured water mole fraction.

498 The efficiency of water correction by this function was assessed in two ways: i) by comparing

499 the water vapor content in standard air measured by this analyzer with similar measurements

500 by the NDIR analyzer and ii) by comparing the oxygen mixing ratios between non-dried

501   ambient air measured and corrected for water dilution by the CRDS analyzer with dried air

502   measured using a paramagnetic analyzer.

503   Figure 14 shows the water vapor content for standard gases measured continuously for

504   two days by the CRDS and the NDIR analyzers. Note that the two data sets are manually

505   fitted to each other as the measured water values by the NDIR analyzer are not calibrated.

506   Based on these plots, the two analyzers are in very good agreement although there are small

507   differences during very dry conditions (low water content).

508   The water correction test was conducted by measuring dried ambient air (Figure 15a)

509   into both analyzers as well as allowing non-dried air to the CRDS analyzer only (Figure 15b)

510   and comparing the difference in O_2 measurements in both cases. Figures 15c & 15d show the

511   water contents of dried ambient air measured in both analyzers (note that the CRDS uses its

512   in-built water correction function). The measurements of the Paramagnetic analyzer were

513   scaled to ppm units by applying the correlation equation obtained from the six standard gas

514   measurements of the two analyzers (Fig. A.1). Note that the CRDS measurements were

515   corrected for the observed drift using the polynomial fit to the two standard gas measurements

516   stated above.

517   In the first period of the measurement when both analyzers measured dried ambient

518   air, the absolute differences between the 1-minute averages measured over two days by the

519   two analyzers were mostly within 15 ppm and symmetrically distributed around zero.

520   However, when wet air was admitted to the CRDS analyzer and the in-built water correction

521   was applied, a stronger variability was observed in the calculated differences. This implies

522   stronger short term variability in the CRDS analyzer measurement values (as nothing was

523   changed for the Paramagnetic measurement system) when wet samples were analyzed. The

524   more negative values in the differences can also be associated with overestimation of the O_2

525   mixing ratios by the CRDS originating from an overestimated water correction. However,

526   detailed evaluation of the analyzer's water correction function is beyond the scope of this

527   study.

528   **3.3. Field Measurements**

529   After a series of tests at University of Bern, we conducted multiple field measurements

530   at the High Altitude Research Station Jungfraujoch and the Beromünster tall tower sites in

531   Switzerland described below.

532   3.3.1. Tests at the High Altitude Research station Jungfraujoch

533   The High Alpine research station Jungfraujoch is located on the northern ridge of the

534   Swiss Alps (46° 33′ N, 7° 59′ E) at an elevation of 3580 m a.s.l. It is one of the global

535   atmospheric watch (GAW) stations well-equipped for measurements of numerous species and

536   aerosols. The site is above the planetary boundary layer most of the time due to its high

537   elevation (Henne et al., 2010; Zellweger et al., 2003). However, thermally uplifted air from

538   the surrounding valleys during hot summer days or polluted air from the heavily industrialized

539   northern Italy may reach at this site (Zellweger et al., 2003). The Division of Climate and

540   Environmental Physics at the University of Bern has been monitoring CO_2 and O_2 mixing

541   ratios at this site based on weekly flask sampling and continuous measurements since 2000

542   and 2004, respectively (Schibig et al., 2015). The CO_2 mixing ratio is measured using a

543   commercial NDIR analyzer (S710 UNOR, SICK MAIHAK) while O_2 is measured using the

544   Paramagnetic sensor (PM1155 oxygen transducer, Servomex Ltd, UK) and fuel cells (Max-

545   250, Maxtec, USA) embedded within a home-built controlling unit. Similar to the comparison

546   tests at the University of Bern, we have conducted parallel measurements between the CRDS

547   analyzer and the paramagnetic cell at this high altitude site during 03 – 14 February 2017. The

548   measurement of ambient air at the Jungfraujoch system is composed of sequential switching

549   between a low span (LS) and high span (HS) calibration gases followed by a target gas (T)

550   measurement (once a day) to evaluate the overall system performance and finally a working

551   gas (WG) measurement before switching back to ambient air.

552   Figure 16 (top panel) shows the calibrated 1-minute averaged O_2 mixing ratios

553   measured at this high altitude site in comparison with the Paramagnetic oxygen analyzer

554   already available at the site. While a strong variability was observed during the measurement

555   period of 10-days by both analyzers, a very good agreement was observed between them.

556   Figure 16 (bottom panel) shows the absolute difference of 1-minute averages in

557   atmospheric O_2 measured at Jungfraujoch between the two analyzers which are mostly within

558   ±5 ppm range (but sometimes going as high as ±10 ppm) without an offset. However, for

559   generally reported 10-minutes, half-hourly or hourly means these values correspond to < 1.5

560   ppm, < 1 ppm and < 0.65 ppm.

561   3.3.2. Tests at the Beromünster tall tower site

562   The Beromünster tower is located near the southern border of the Swiss Plateau, the

563   comparatively flat part of Switzerland between the Alps in the south and the Jura mountains

564   in the northwest (47° 11′ 23″ N, 8° 10' 32″ E, 797 m a.s.l.), which is characterized by intense

565   agriculture and rather high population density. A detailed description of the tower

566   measurement system as well as a characterization of the site with respect to local

567   meteorological conditions, seasonal and diurnal variations of greenhouse gases, and regional

568   representativeness can be obtained from previous publications (Berhanu et al., 2016; Berhanu

569   et al., 2017; Oney et al., 2015; Satar et al., 2016). The tower is 217.5 m tall with access to five

570   sampling heights (12.5 m, 44.6 m, 71.5 m, 131.6 m, 212.5 m) for measuring CO, CO_2, CH_4

571   and H_2O using Cavity Ring Down Spectroscopy (Picarro Inc., G-2401). By sequentially

572   switching from the highest to the lowest level, mixing ratios of these trace gases were

573 recorded continuously for three minutes per height, but only the last 60 seconds were retained

574 for data analysis. The calibration procedure for ambient air includes measurements of

575 reference gases with high and low mixing ratios traceable to international standards (WMO-

576 X2007 for CO_2 and WMO-X2004 for CO and CH_4), as well as target gas and more frequent

577 working gas determinations to ensure the quality of the measurement system. From two years

578 of data a long-term reproducibility of 2.79 ppb, 0.05 ppm, and 0.29 ppb for CO, CO_2 and

579 CH_4, respectively was determined for this system (Berhanu et al., 2016).

580   Between 15.02.2017 and 02.03.2017, we have connected the new CRDS oxygen

581 analyzer in series with the CO_2 analyzer (Picarro G-2401) and measured the O_2 mixing ratios

582 at the corresponding heights. Similar to the CO_2 measurements, O_2 was also measured for

583 three minutes at each height. During this period, we have evaluated the two features (isotopic

584 mode and concentration mode) of the CRDS analyzer. In the isotopic mode, the CRDS

585 measures the $\delta^{18}O$ values as well as the O_2 concentration while in concentration mode only

586 the latter was measured.

587   During the tests conducted at this tower site, we first evaluated the two operational

588 modes (concentration vs isotopic modes) of the CRDS analyzer. Ambient air measurements

589 on isotopic mode over a 4-days period showed a strong variability in the measured oxygen

590 mixing ratios and it was not possible to distinguish the variability in the O_2 mixing ratios

591 among the five height levels. The calculated 1-minute standard error for ambient air

592 measurements was as high as 10 ppm while a standard error of less than 1 ppm was

593 determined from similar measurements in the concentration mode. Additionally, comparing

594 the O_2 values between the two modes, frequent short time variation in ambient air O_2 (~ 200

595 ppm) was observed in the isotope mode measurements while the variation in the concentration

596 mode is significantly smaller (~ 30 ppm). This precision degradation is due to the weaker ^{16}O

oxygen line used for the isotopic mode, and the fact that far more ring-downs are collected on the rare isotopologue in isotopic mode Hence, we have conducted the remaining test measurements in concentration mode.

As this tower has five sampling height levels, we first followed three minutes of switching per inlet level, which enables four measurements per hour at a given level. However, we noticed hardly any difference among the different levels due to strong short term variability in O_2 mixing ratios between the consecutive heights. Hence, we switched to a longer sampling period of six-minutes per height. Figure 17 shows the diurnal CO_2 and O_2 variations at the lowest (12 m) and highest (212.5 m) sampling heights of the tower. These two heights were selected simply to better illustrate the difference in the mixing ratios. The CO_2 mixing ratios on the top panel show higher values at the 12 m inlet than the highest level most of the day due to its closeness to sources except during the afternoon (11:00 - 17:00 UTC) when both levels show similar but decreasing CO_2 mixing ratios. This is due to presence of a well-mixed planetary boundary layer (PBL) (Satar et al., 2016). The lag in CO_2 peak between the two height levels by about two hours indicates the duration for uniform vertical mixing along the tower during winter 2017. The opposite variability patterns are also clearly visible in the O_2 mixing ratios shown in the lower panel with a clear distinction between the two height levels during early in the morning and in the evening while similar O_2 values were observed in the afternoon. These opposing profiles are expected as CO_2 and O_2 are linearly coupled with a mean oxidation ratio of -1.1 ± 0.05 (Severinghaus, 1995) for land-biospheric processes (photosynthesis and respiration) and -1.44 ± 0.03 for fossil fuel burning (Keeling, 1988b).

Table 2 shows the oxidation ratios derived as the slopes of the linear regression between CO_2 and O_2 mixing ratios at the different height levels measured on 25 February

621 2017. Accordingly, height dependent slopes were observed with a slope of -0.98 ± 0.06 at the

622 lowest level, close to the biological processes induced slope but slightly lower than its mean

623 value. For the highest level, we calculated a slope of -1.60 ± 0.07 a value close to fossil fuel

624 combustion oxidation ratio. Note that depending on fossil fuel type the oxidation ratio can

625 range between -1.17 and -1.95 for coal and natural gas, respectively (Keeling, 1988b). While

626 the slopes derived for the two other levels (44.6 m and 131.6 m) show similar values between

627 the highest and lowest height levels, possibly from mixed sources, the middle level showed a

628 slightly higher slope than these two levels but still in the large range between the lowest and

629 highest inlet heights.

630 3.4. Evaluation of the $\delta^{18}O$ measurements

631   To further evaluate the analyzer's performance in measuring stable oxygen isotopes,

632 we conducted ambient air isotopic composition measurements as well as analyzed a standard

633 gas without CO_2 which has a known $\delta^{18}O$ value. The choice of this CO_2-free air standard gas

634 is twofold: one it has a known $\delta^{18}O$ value and second as it has no CO_2 possible interference

635 from band overlap. For this test three 0.5 L glass flasks were preconditioned and filled with

636 this standard gas to ambient pressure. These flasks were attached before or after the water trap

637 (Fig. 11) and measured similar to ambient air measurements. These measurements were then

638 compared with $\delta(^{34}O/^{32}O)$ values obtained by parallel measurements using our IRMS.

639   Figure 18 shows the $\delta^{18}O$ values of ambient air from the roof top with three

640 consecutive measurements of glass flasks filled with CO_2-free air in-between followed by a

641 fourth flask filled with breath air. An excellent agreement was observed for measurements

642 from both instruments for the three flasks filled with a standard gas. However, the fourth flask

643 with breath air showed a signal opposite to the measurements by the IRMS. As breath air

644 contains large amount of water and CO_2 in addition to O_2, which can possibly interfere with

the CRDS analyzer measurements, we have removed H_2O and CO_2 by using a cryogenic trap (-130 °C) and in an additional experiment using Schütze reagent to remove both CO and CO_2. However, we have not observed any improvement towards an agreement with the IRMS measurements. Therefore, any other gas component in the breath air must be relevant for the interference. Based on the absorption lines in the spectral range of the instrument (7878 cm^{-1}) retrieved from HITRAN database, we expect interference either from carbon monoxide (now excluded by the tests) or methane or VOCs including acetone, ethanol, methanol or isoprenes, all of which have been measured in breath air (Gao et al., 2017; Gottlieb et al., 2017; Mckay et al., 1985; Ryter and Choi, 2013; Wolf et al., 2017). Further investigations have to shed light on these interferences in order to take corresponding action to surpass these shortcomings in the isotope analysis based on cavity ring-down spectroscopy.

4. Conclusions

We have thoroughly evaluated the performance of a new CRDS analyzer which measures O_2 mixing ratios and isotopic composition combining laboratory and field tests. Even if a drift in the analyzer was observed at the beginning of this study, which if it appears can be easily corrected by calibration, the recent analyzers built by the manufacturer did not show such instrumental drift. However, prior tests are recommended to see the analyzer's stability.

The T-split tests for the current measurement setup based on the measurements of two standard gases showed a difference within the measurement uncertainty. However, this effect may become significant while applying larger splitting ratios and we recommend conducting further experiments to accurately quantify this influence for larger splitting ratios.

We have observed a strong influence of dilution in the measured O_2 values during the presence of high CO_2 mixing ratios. Even if such an influence may not be critical for the

669   present study, such an effect might be significant in other studies where higher CO_2 mixing

670   ratios might be present and we recommend following a correction strategy based on parallel

671   CO_2 measurements. This also applies for more accurate analysis.

672   The water correction applied by the instrument's in-built function seems to sufficiently

673   correct for the water vapor influence. However, a larger variability of the difference was

674   observed between the CRDS analyzer and the Paramagnetic cell when dried samples were

675   used in both systems. This can possibly be due to an overcorrection by the water correction

676   function of the CRDS analyzer when dried samples were used. This is particularly true for the

677   very low water vapor range (< 100 ppm). However, we believe that it is important to further

678   investigate this issue and identify an improved water correction strategy.

679   Based on the analysis of O_2 mixing ratios in the concentration and isotopic modes, we

680   have observed about a significant decrease in precision (about ten-fold) in the latter

681   measurement mode. The measured $\delta^{18}O$ values for the standard air by the CRDS analyzer are

682   in excellent agreement with the IRMS values. However, such measurements for a breath air

683   showed a contrasting signal, possibly due to interference from other gases as breath air

684   contains CO_2, CH_4 and CO in addition to oxygen. Hence, we recommend further investigation

685   on such possible contaminants and how to possibly remove them while conducting ambient

686   air measurements. However, we believe that this analyzer can be used for tracer experiments

687   where artificially enriched isotopes are used to study biological processes such as

688   photosynthesis in plants using isotopically labelled CO_2 and H_2O.

689

690

691

692

Acknowledgement

We would like to thank ICOS-RI and the Swiss National Science Foundation (SNF) for funding ICOS-CH (20FI21_148994, 20FI21_148992). We are also grateful to the International Foundation High Alpine Research Stations Jungfraujoch and Gornergrat. The measurement system at the Beromünster tower was built and maintained by the CarboCount-CH (CRSII2_136273) and IsoCEP (200020_172550) projects both funded by SNF.

Table 1. Assigned mixing ratios of standard gases used in this study and their corresponding values measured by the NDIR, CRDS and IRMS at the University of Bern. [1]The assigned values are based on measurements from different institutions (University of Bern (UB), Scripps or NOAA, see column cylinder name). [2]Measurements are on the Bern scale for CO_2 and O_2. The Bern scale is shifted by +550 per meg. [3]Values on the Scripps scale.

Cylinder name	Assigned CO_2 (ppm) [1]	Assigned O_2 (per meg) [1]	CO_2-IRMS (ppm) [2]	CO_2-NDIR (ppm) [2]	O_2-IRMS (per meg) [2]	O_2-Paramagnetic (per meg) [2]	O_2-CRDS (per meg)[2]
ST-1 LUX3576-UB	427.47	-1026	427.47	427.59	-1026	-1070	-1057
ST-2 LK922131-UB	368.09	599	368.09	367.82	599	560	590
ST-3 CA07045-Scripps	382.303	-271.6	382.50	381.99	278 (-272.2)[3]	302	281
ST-4 CA07043-Scripps	390.528	-476.4	390.69	390.15	71 (-479.5)[3]	66	63
ST-5 CA07047-Scripps	374.480	-807.7	374.70	374.17	-253 (-803.3)[3]	-212	-233
ST-6 CA04556-NOAA	192.44	-3410	191.21	191.64	-3410	-2905	-3013
ST-7 CA06943-	2699.45	-		2612.80	-	-2691	-3369

NOAA						
ST-8 LK76852-UB	411.49	37794	411.49	406.25	37794	34513	36017

724

725

726 Table 2. The CO_2 and O_2 correlation coefficients at the different height levels derived using

727 the least square fit and the correlation coefficients (r^2). Uncertainties are calculated as

728 standard error of the slope.

Height	Oxidation Ratios ($O_2:CO_2$)
12.5 m	-0.98 ± 0.06 (0.48)
44.6 m	-1.29 ± 0.07 (0.50)
71.5 m	-1.49 ± 0.08 (0.47)
131.6 m	-1.23 ± 0.05 (0.55)
212.5 m	-1.60 ± 0.07 (0.61)

729

730

731

732

733

734

735

736
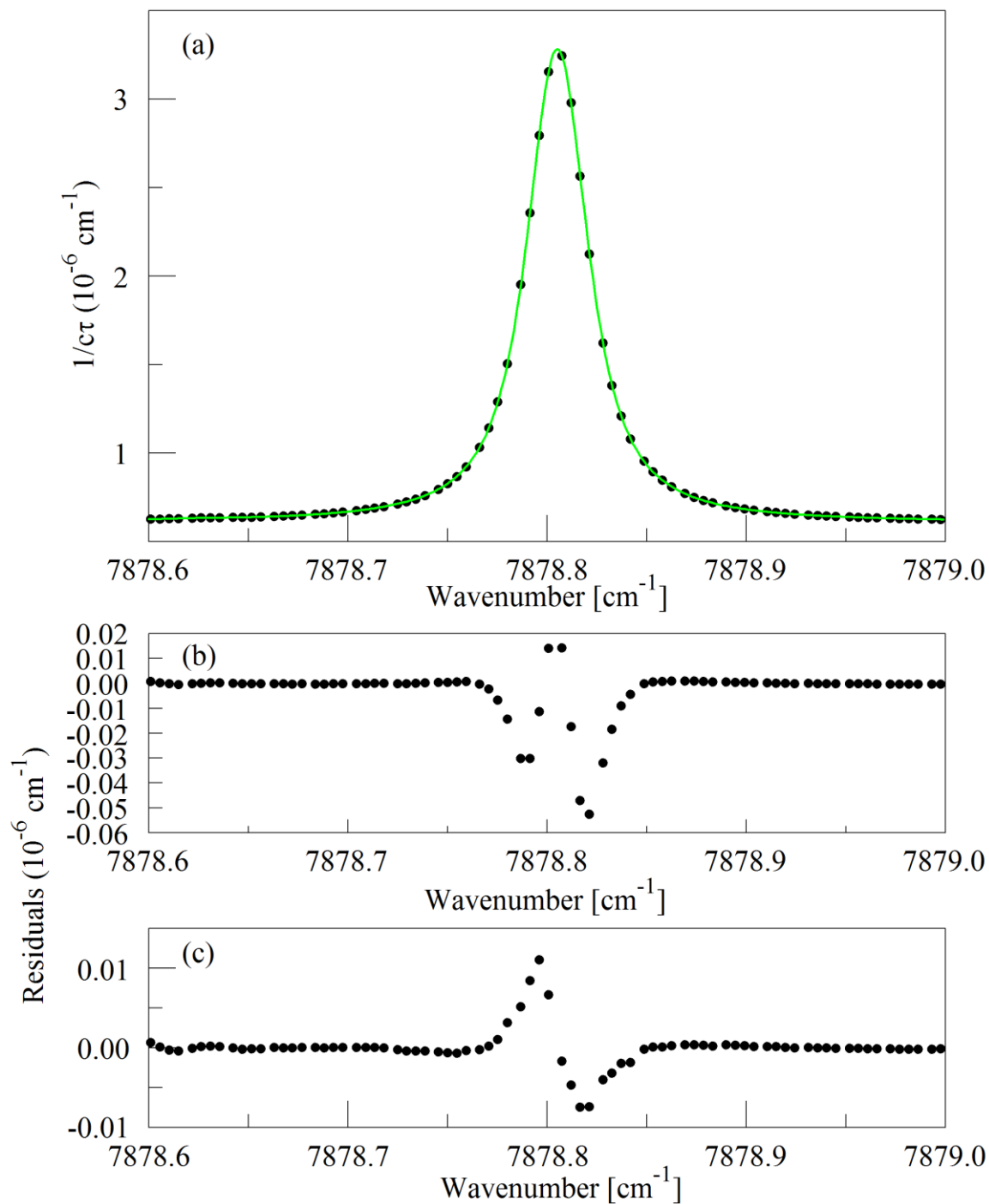
738

739   Figure 1.

740   The top panel (a) shows the raw data (points) and the best-fit Galatry function (solid line). Residuals

741   of the Voigt fit are shown in panel (b) and residuals of the Galatry fit are shown in panel (c)

742
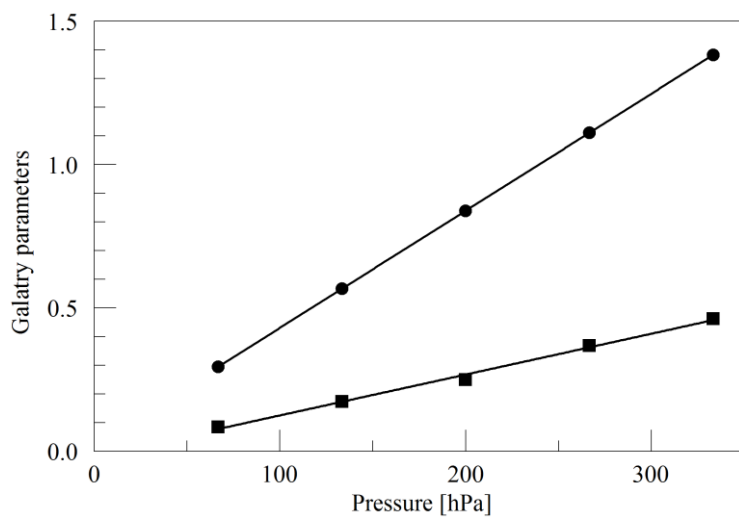
743

744   Figure 2. Best-fit values for the Galatry parameters of the Q13Q13 line of O_2, as a function of

745   pressure. The line broadening parameter y is represented by circles and the line narrowing

746   parameter z by squares. The solid lines are linear fits to the measurements. The best-fit offset

747   and slope are 0.0227 and 0.004082 hPa^{-1} for y, and -0.0169 and 0.001424 hPa^{-1} for z.
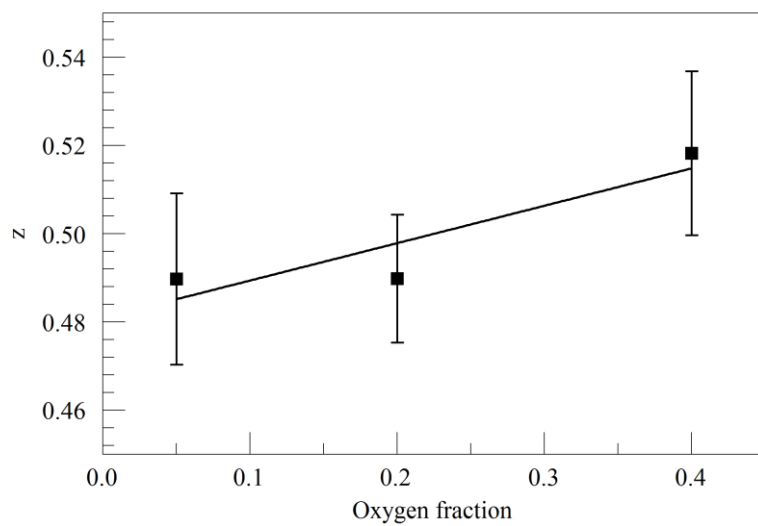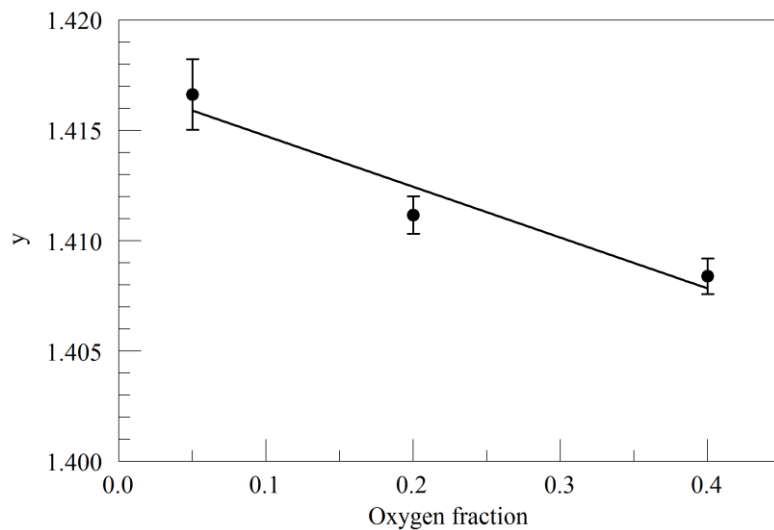
748

749   Figure 3. Galatry parameters of the Q13Q13 line of O_2 at 340 hPa and 45° C as a function of

750   O_2 mole fraction in binary O_2 - N_2 mixtures.

751   The linear fits to the data are $y = 1.417 - 0.023 \times f_{O2}$ and $z = 0.481 + 0.085 \times f_{O2}$.
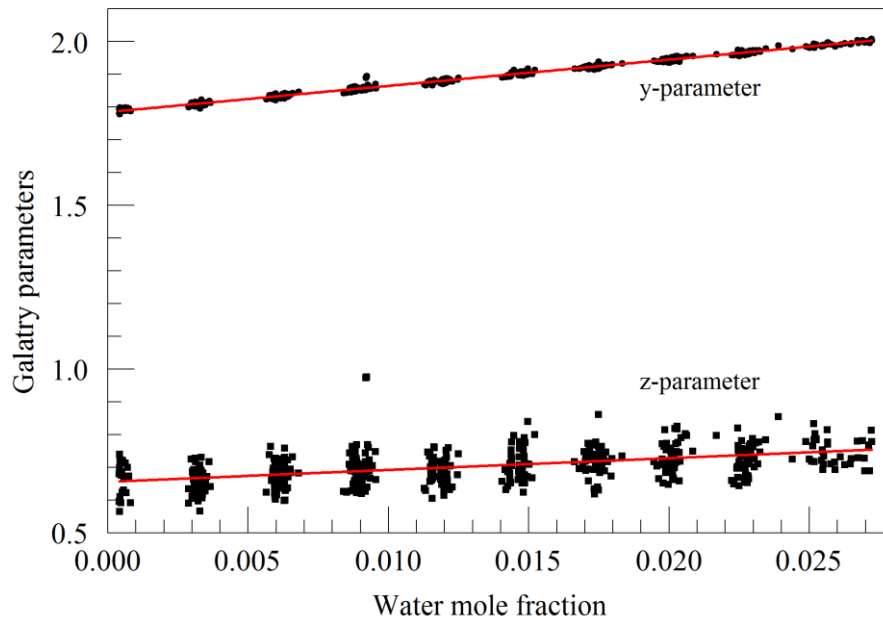
752

753 Figure 4. Galatry parameters of the 7816.75210 cm^{-1} water line in air at 340 hPa and 45° C as

754 a function of water mole fraction. Black points are from measurements and red lines are

755 linear fits: $y = 1.7846 + 8.01 \times f_{H2O}$ and $z = 0.656 + 3.60 \times f_{H2O}$.
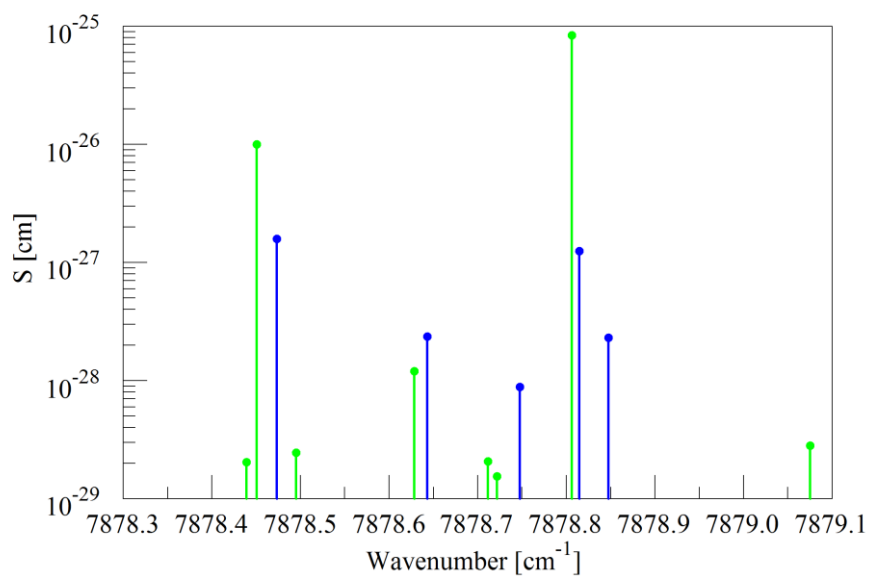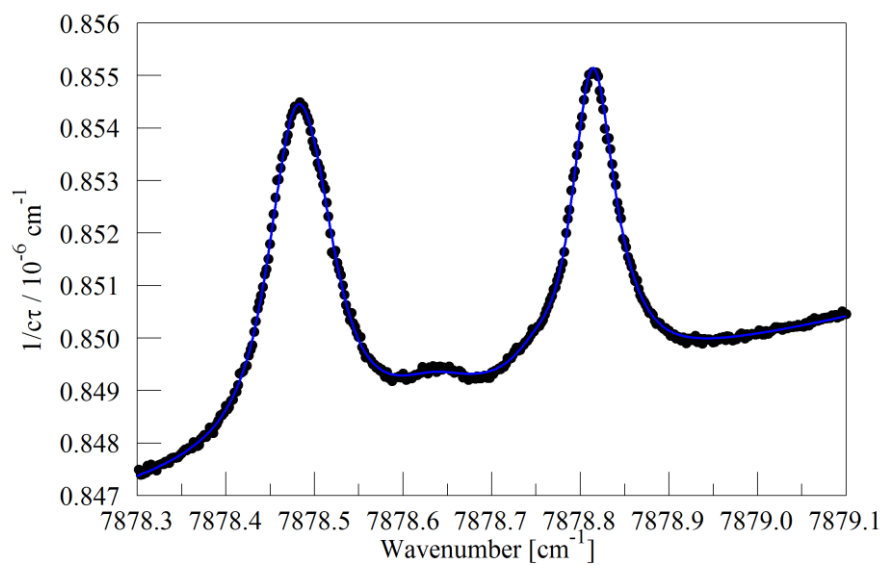
756

757 Figure 5. Upper panel: spectrum of water in nitrogen (points) and fit to Voigt model (blue

758 curve). Lower panel: Oxygen (green) and water (blue) lines in the Hitran database.
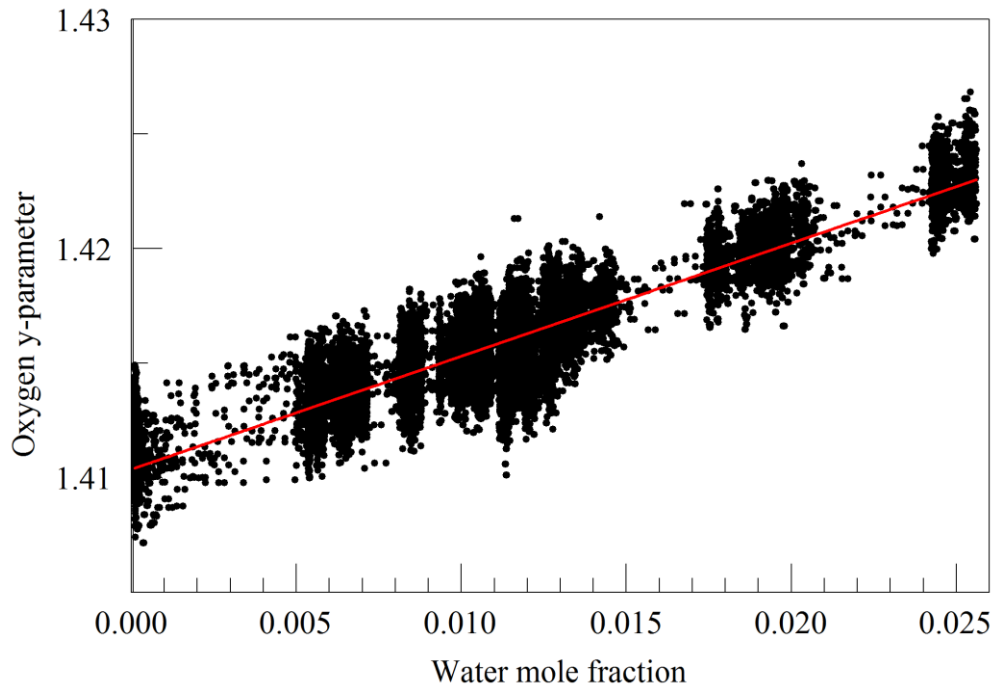
759

760 Figure 6.   Galatry collisional broadening parameter of the oxygen Q13Q13 line at 340 hPa

761 and 45° C versus water mole fraction. Black points are from measurements and the red line is

762 a linear fit: $y = 1.4109 + 0.467 f_{H2O}$.

763

764

765

766
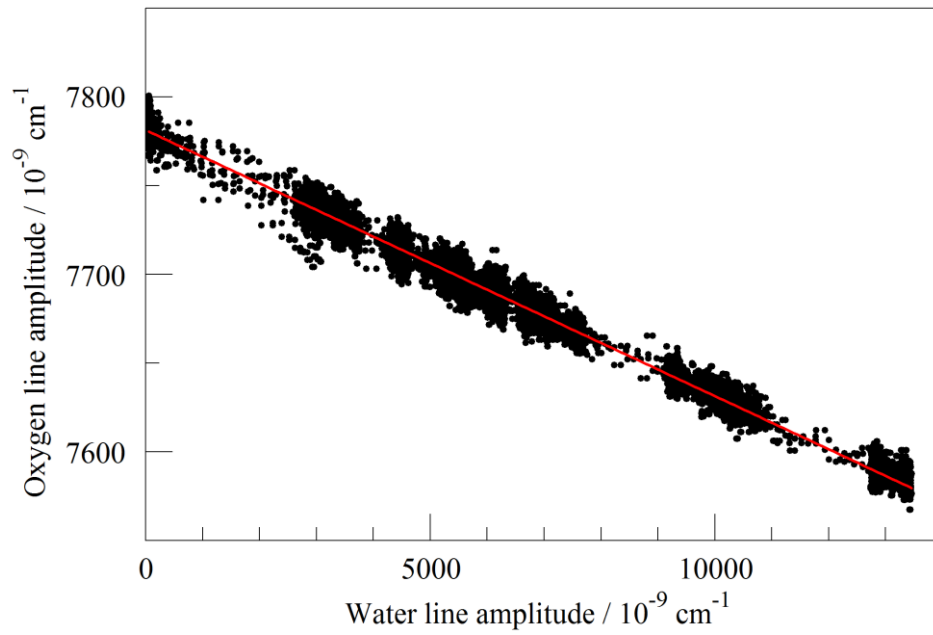
767

768

769 Figure 7. Measured absorption line amplitudes for oxygen and water vapor for water vapor

770 mixing ratios ranging from nearly 0 to 0.025. Black points are from measurements and the

771 red line is a linear fit: with intercept 7.78001×10^{-6} cm^{-1} and slope -0.014807.

772

773

774

775

776

777
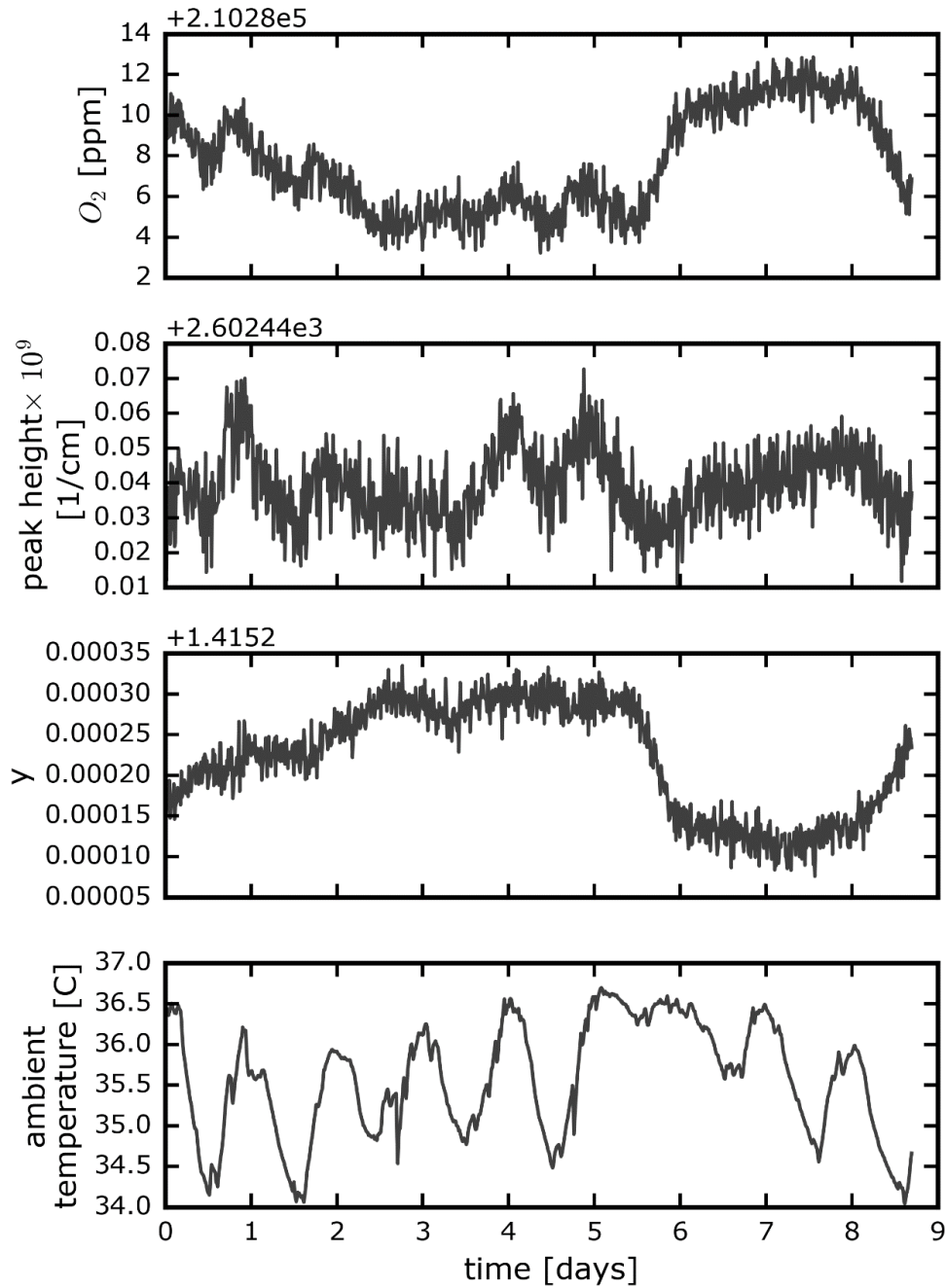
Figure 8. Time series from a measurement of a single tank over about a week. The four panels show the water-corrected oxygen concentration, the absorption peak loss minus the baseline loss, the measured Lorentzian broadening factor, and the ambient temperature (measured in the instrument housing), respectively. A windowed average of 300 seconds was applied to all four data sets.
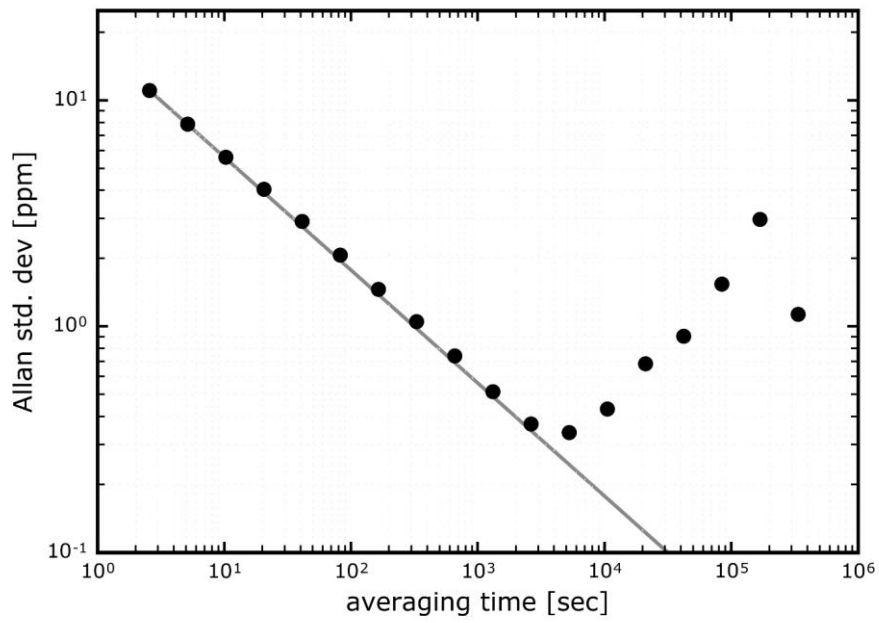
783

784   Figure 9. Precision of O_2 mole fraction measured from a tank of synthetic air. Filled circles

785   are measurements and the line shows the ideal $\tau^{-1/2}$ dependence.

786

787

788

789

790

791

Figure 10. Precision of $\delta(^{18}O)$ measured from a tank of synthetic air. Filled circles are

measurements and the line shows the ideal $\tau^{-1/2}$ dependence.
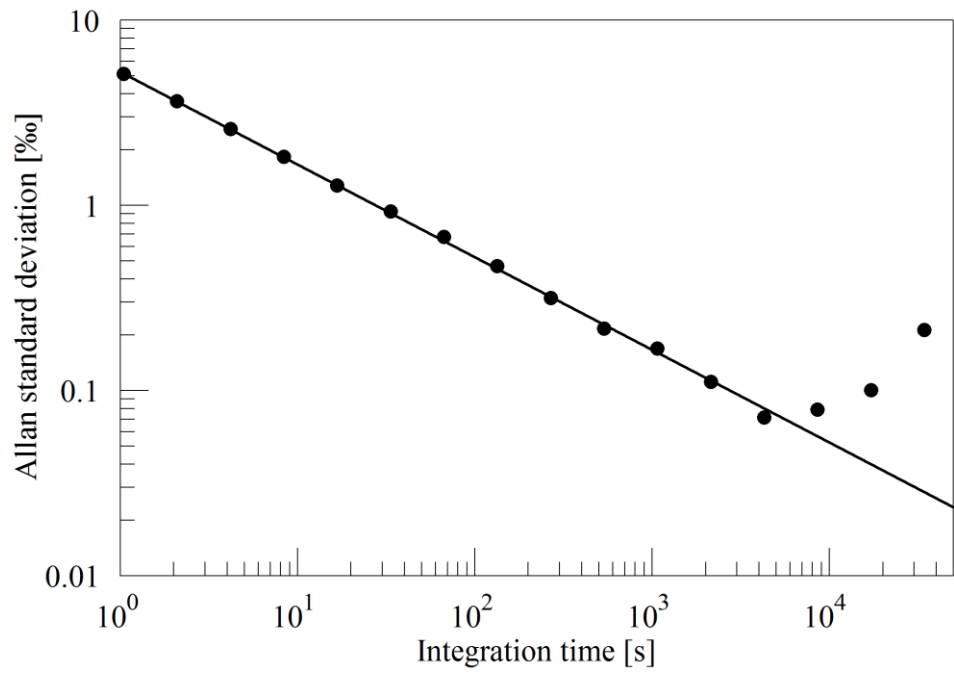
794

795

796

797

798

799

800

801
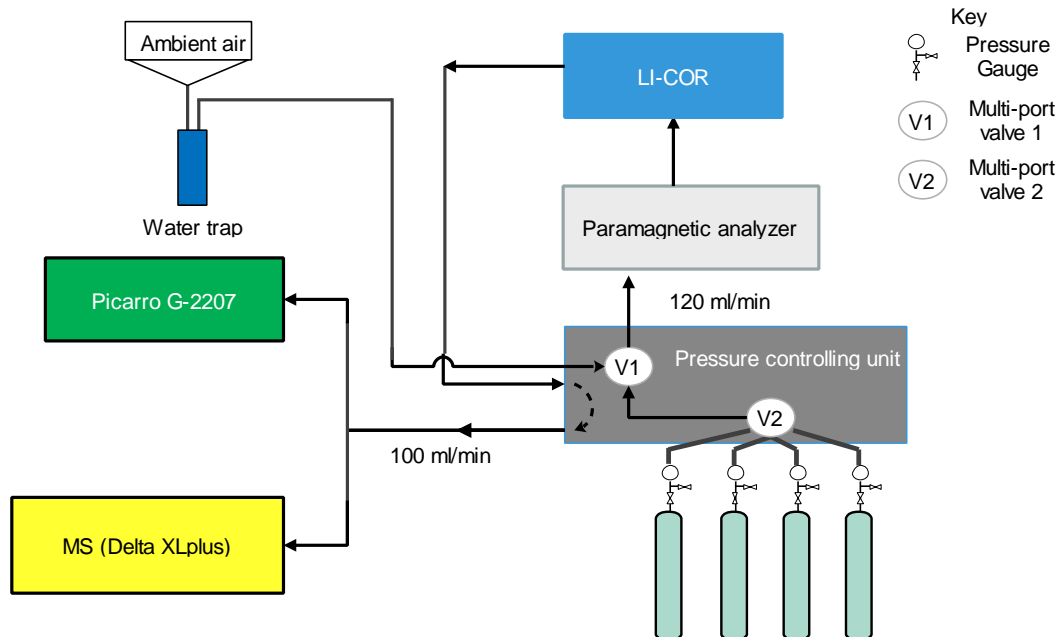
802

803   Figure 11. Schematics of the measurement system used to compare the Picarro analyzer with

804   the Mass Spectrometer at Bern.

805

806

807

808

809

810

811

812

813
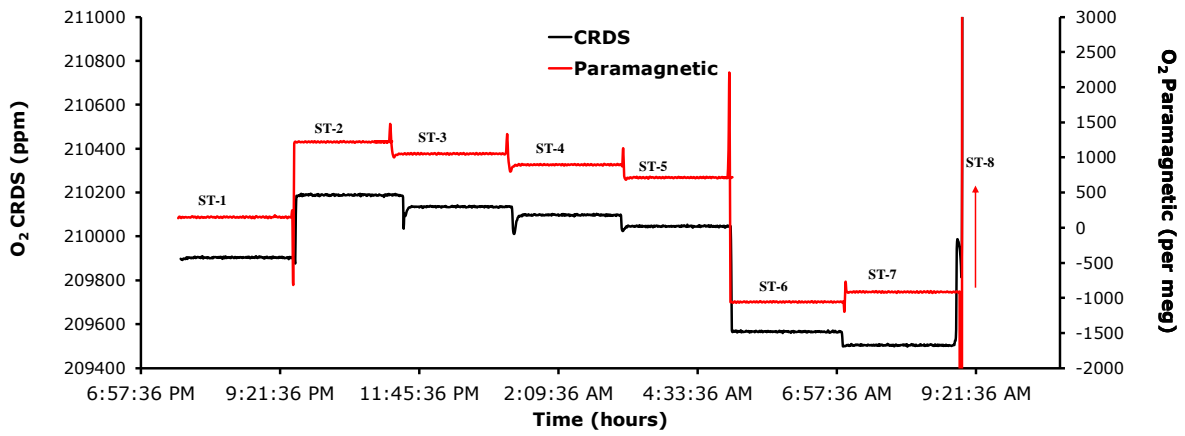
Figure 12. Comparison of oxygen mixing ratios for the seven standard gases measured using the CRDS analyzer (black) and the Paramagnetic sensors (red).

832
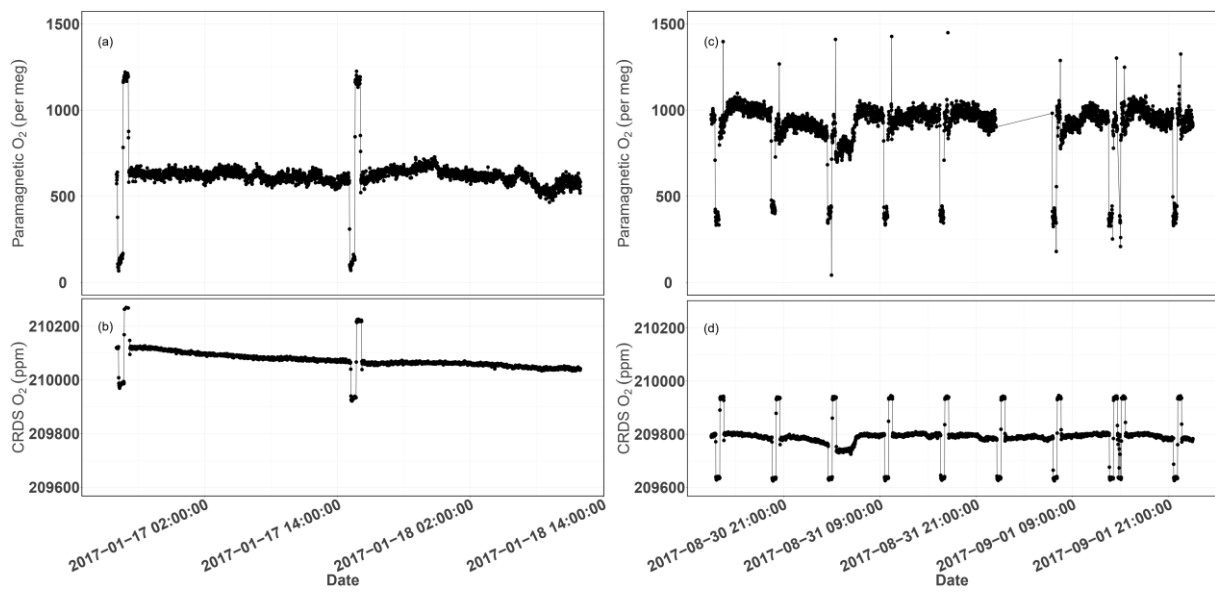
834 Figure 13. Parallel ambient air measurements by the Paramagnetic and CRDS analyzers at the

835 beginning of the testing period (Panels a & b, January 2017) and the second phase of testing

836 (Panels c & d, September 2017). The spikes are measurements from the two standard gases

837 bracketing the ambient air values.

838

839

840

841

842

843

844

845

846

847

848

849
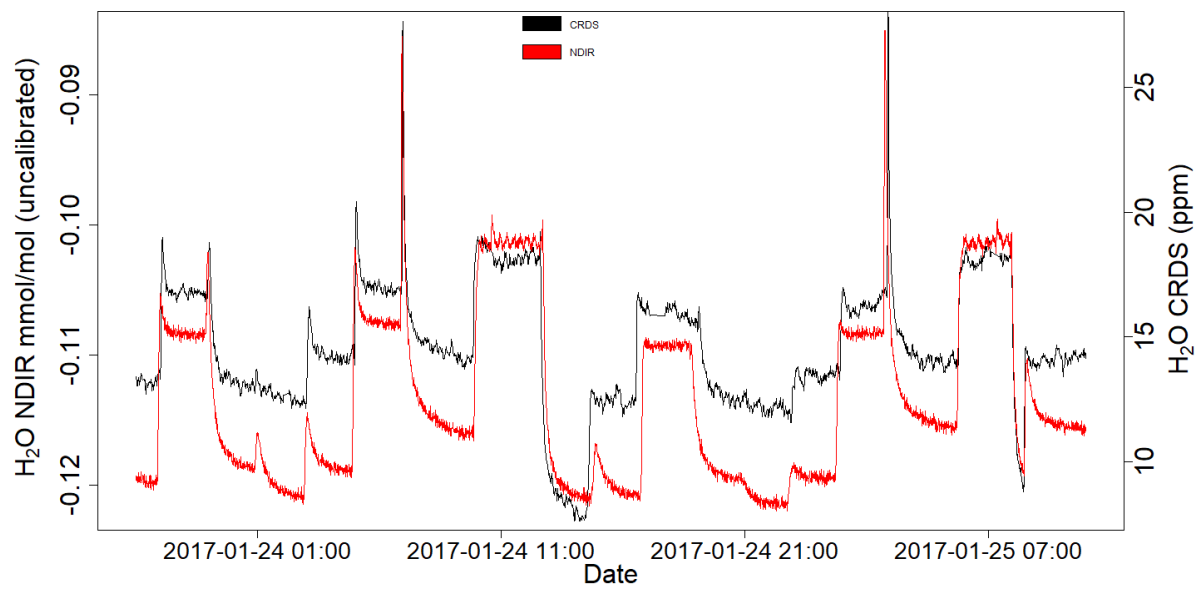
850
851 Figure 14. Parallel water vapor measurements for a dried ambient air by both the NDIR and

852 CRDS analyzers. Note that the water values from the NDIR analyzer are not calibrated.

853

854

855

856

857

858

859

860

861

862

863

864
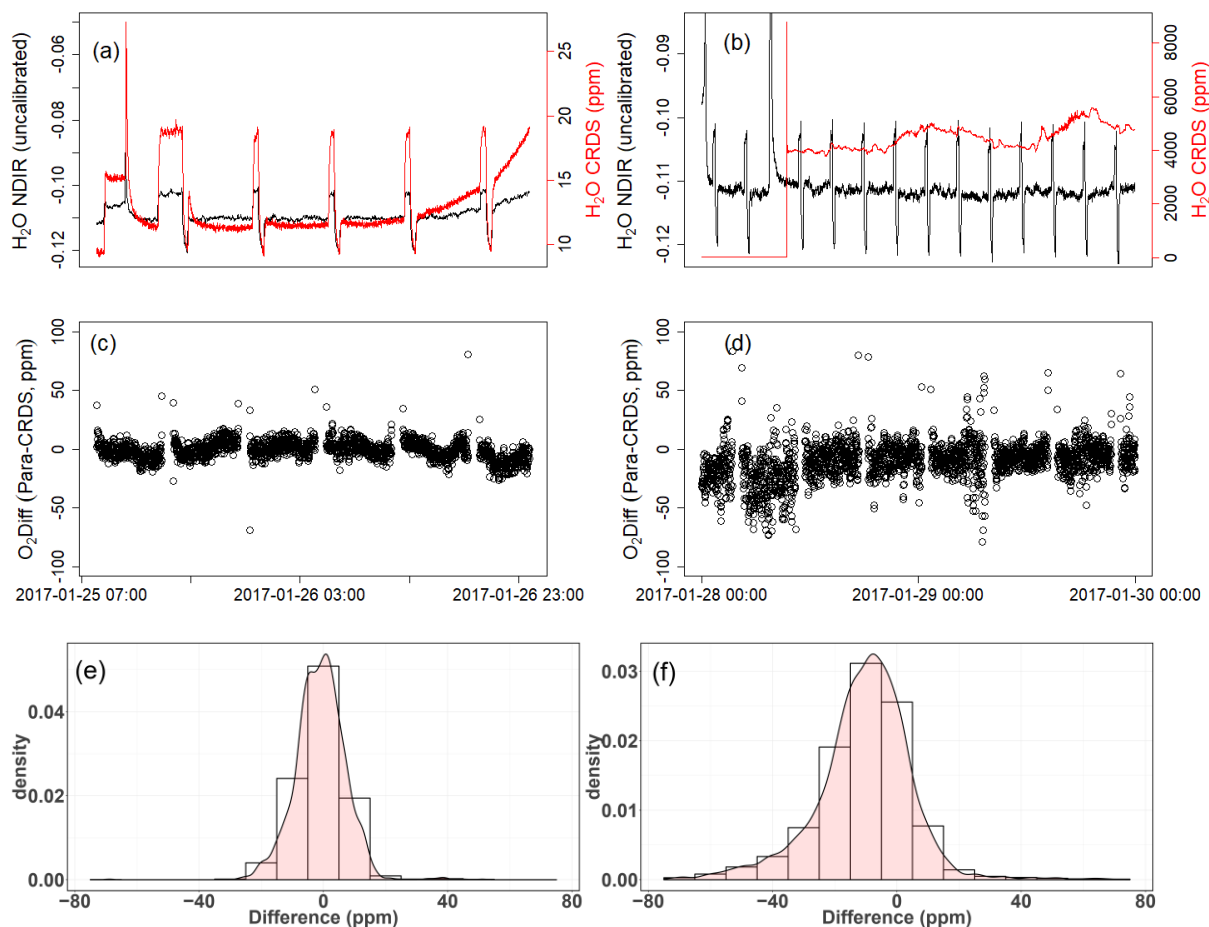
866 Figure 15. Results of water correction tests. Water measurements of the NDIR (left scale) for

867 dry conditions (a,b) and the CRDS analyzer (right scale) for dry (a) and wet (b) conditions.

868 The difference in oxygen measurements between the Paramagnetic and the CRDS instrument

869 using the built-in water correction for the CRDS values under dry (c) and wet (d) conditions.

870 Panels (e) and (f) show the population density functions.

871

872

873

874

875

876

877
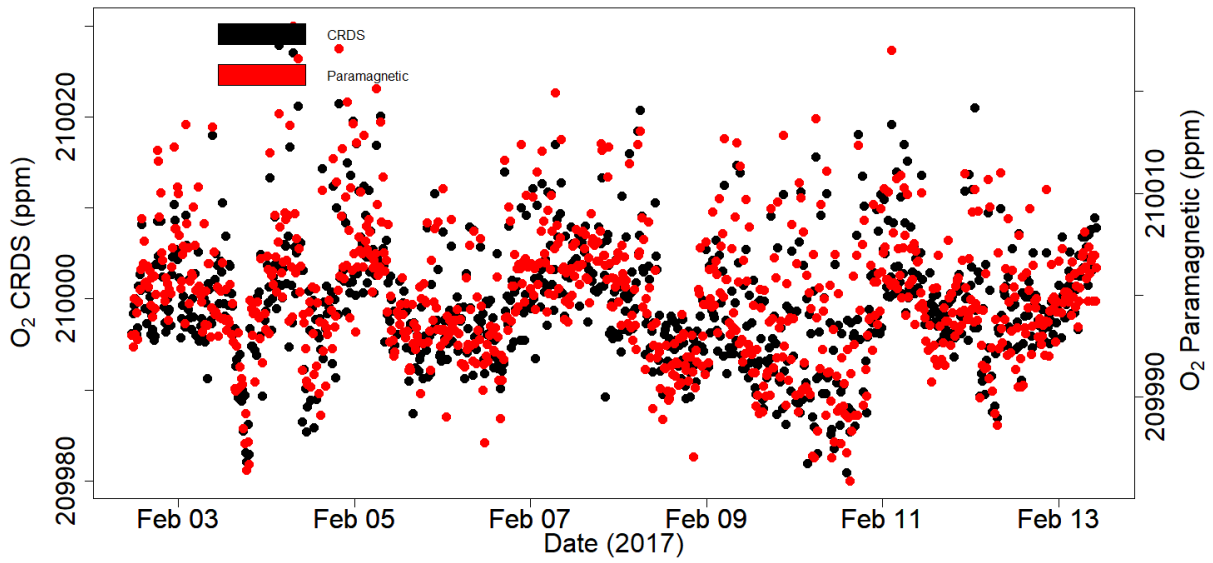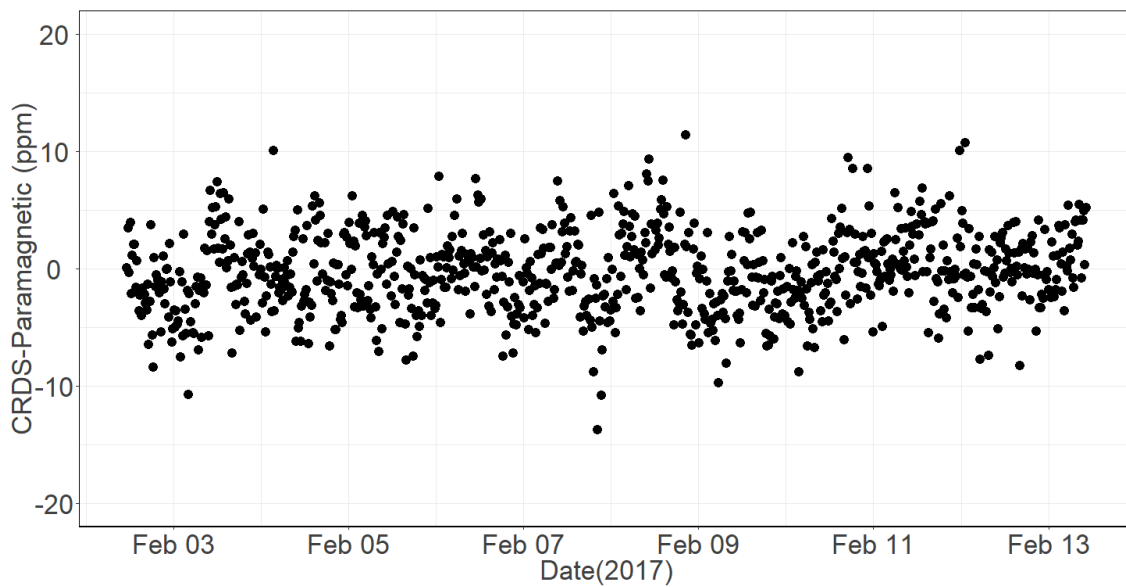
Figure 16. Calibrated ambient air oxygen measurements (1-minute average) at the
Jungfraujoch site using the CRDS and Paramagnetic analyzers both in ppm units (a) and the
absolute difference between the two measurements in ppm (b) by matching time stamps.

881

882

883

884
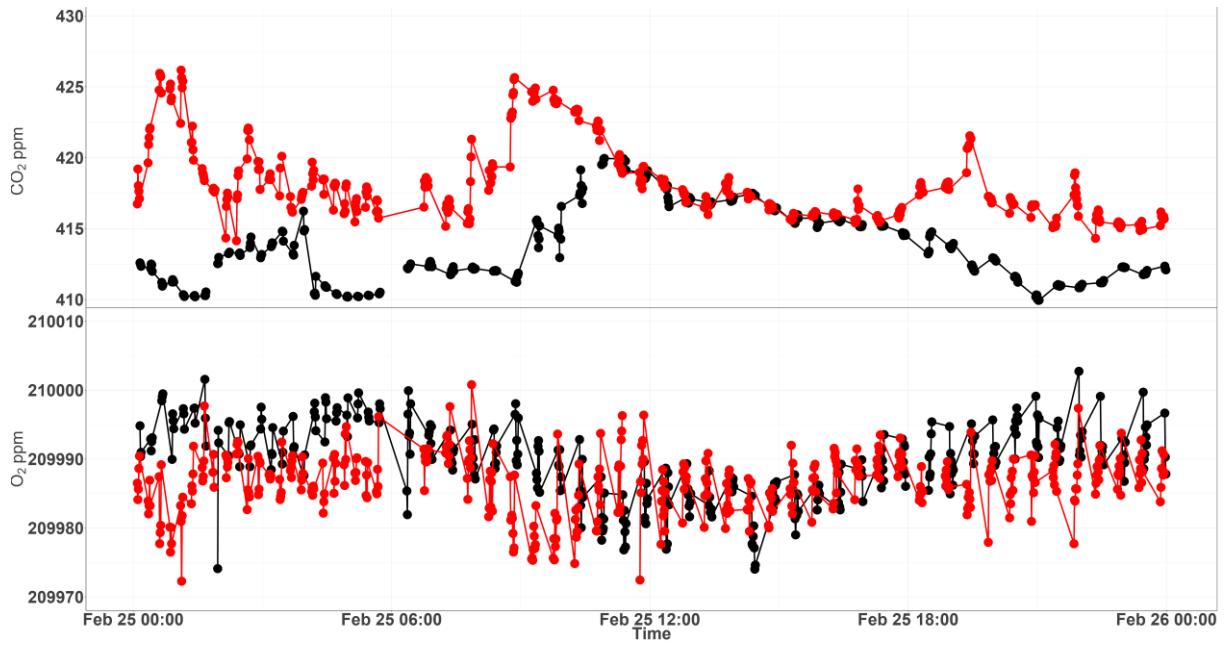
885

886   Figure 17. Diurnal variations of CO_2 (top) and O_2 (bottom) measurements from the 12 m (red)

887   and the 212.5 m (black) height levels at Beromünster tower.

888

889

890

891

892

893

894

895

896

897
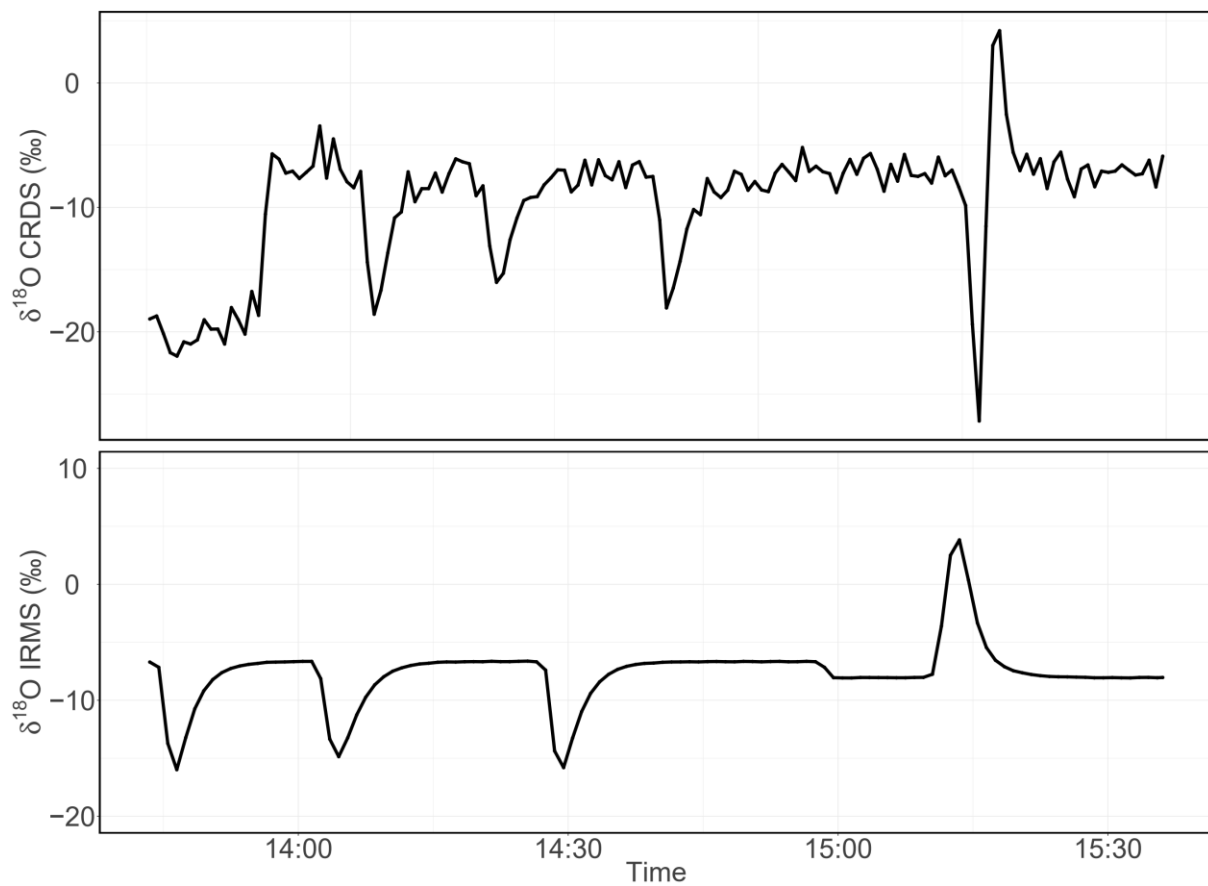
898

899 Figure 18. Consecutive $\delta^{18}O$ measurements of a standard gas (CO_2-free air) filled into three

900 flasks followed by measurement of breath air using the CRDS analyzer (top) and IRMS

901 (bottom). These measurements were carried out in the middle of ambient air measurements.

902

903

904

905

906

907

908

909 **Appendix A.**

910 **Additional plots**

911
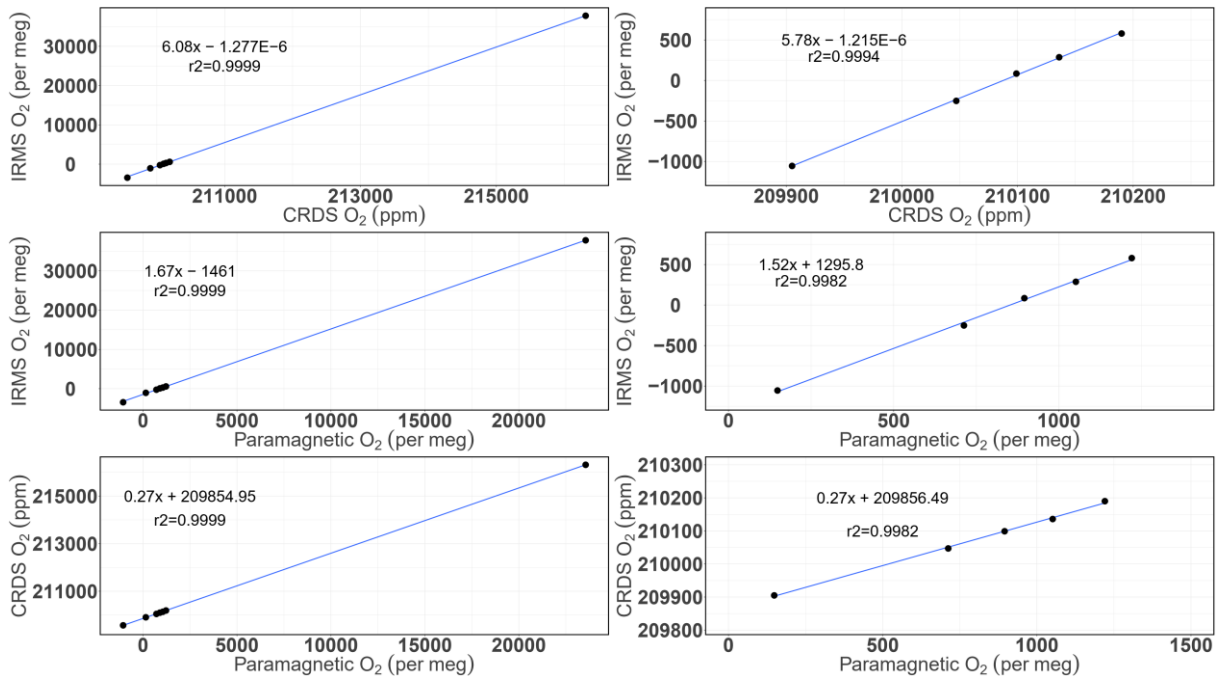
912

913 Figure A.1. Correlations between the O_2 mixing ratios measured by the CRDS and
914 Paramagnetic analyzers with the mass spectrometric measurements (uncalibrated values). The
915 left panels are for all the cylinders measured (standards 1 to 8) while the right ones are after
916 zooming only to standards 1-5.

917

918

919

920

921

922

923

924 **References**

925 Battle, M., Bender, M. L., Tans, P. P., White, J. W. C., Ellis, J. T., Conway, T., and Francey, R. J.: Global

926 carbon sinks and their variability inferred from atmospheric O-2 and delta C-13, Science, 287, 2467-

927 2470, 2000.

928 Bender, M. L., Tans, P. P., Ellis, J. T., Orchardo, J., and Habfast, K.: A High-Precision Isotope Ratio

929 Mass-Spectrometry Method for Measuring the O-2 N-2 Ratio of Air, Geochim Cosmochim Ac, 58,

930 4751-4758, 1994.

931 Berhanu, T. A., Satar, E., Schanda, R., Nyfeler, P., Moret, H., Brunner, D., Oney, B., and Leuenberger,

932 M.: Measurements of greenhouse gases at Beromünster tall tower station in Switzerland, Atmos.

933 Meas. Tech. , 9, 2016.

934 Berhanu, T. A., Szidat, S., Brunner, D., Satar, E., Schanda, R., Nyfeler, P., Battaglia, M., Steinbacher,

935 M., Hammer, S., and Leuenberger, M.: Estimation of the fossil-fuel component in atmospheric CO2

936 based on radiocarbon measurements at the Beromünster tall tower, Switzerland, Atmos. Chem.

937 Phys. Discuss., 2017, 1-33, 2017.

938 Crosson, E. R. J. A. P. B.: A cavity ring-down analyzer for measuring atmospheric levels of methane,

939 carbon dioxide, and water vapor, 92, 403-408, 2008.

940 Filges, A., Gerbig, C., Rella, C. W., Hoffnagle, J., Smit, H., Krämer, M., Spelten, N., Rolf, C., Bozóki, Z.,

941 Buchholz, B., and Ebert, V.: Evaluation of the IAGOS-Core GHG Package H2O measurements during

942 the DENCHAR airborne inter-comparison campaign in 2011, Atmos. Meas. Tech., 11, 5279–5297,

943 2018, https://doi.org/10.5194/amt-11-5279-2018. Gao, F., Zhang, X., Zhang, X., Wang, M., and Wang,

944 P.: Virtual electronic nose with diagnosis model for the detection of hydrogen and methane in breath

945 from gastrointestinal bacteria, 28-31 May 2017 2017, 1-3.

946 Gordon, E., Rothman, S., Hill, C., Kochanov, V., Tan, Y., Bernath, P., Birk, M., Boudon, V., Campargue,

947 A., Chance, K., Drouin, J., Flaud, J., Gamache, R. R., Hodges, J., Jacquemart, D., Perevalov, I., Perrin, A.,

948 Shine, P., Smith, M., Tennyson, J., Toon, G., Tran, H., Tyuterev, G., Barbe, A., Császár, G., Devi, M.,

949   Furtenbacher, T., Harrison, J., Hartmann, J., Jolly, A., Johnson, J., Karman, T., Kleiner, I., Kyuberis, A.

950   A., Loos, J., Lyulin, M., Massie, S., Mikhailenko, S., Moazzen-Ahmadi, N., Muller, S., Naumenko, O. V.,

951   Nikitin, A. V., Polyansky, O. L., Rey, M., Rotger, M., Sharpe, S., Sung, K., Starikova, E., Tashkun, S.,

952   Auwera, J., Wagner, G., Wilzewski, J., Wcisło, P., Yu, S., and Zak, E. J.: The HITRAN2016 molecular

953   spectroscopic database, 203, 3 - 69, 2017.

954   Goto, D., Morimoto, S., Ishidoya, S., Aoki, S., and Nakazawa, T.: Terrestrial biospheric and oceanic

955   CO_2 uptake estimated from long-term measurements of atmospheric CO_2 mole fraction, $\delta 13C$ and

956    $\delta(O_2/N_2)$ at Ny-Ålesund, Svalbard, Journal of Geophysical Research: Biogeosciences, doi:

957   10.1002/2017JG003845, 2017. n/a-n/a, 2017.

958   Gottlieb, K., Le, C. X., Wacher, V., Sliman, J., Cruz, C., Porter, T., and Carter, S.: Selection of a cut-off

959   for high- and low-methane producers using a spot-methane breath test: results from a large north

960   American dataset of hydrogen, methane and carbon dioxide measurements in breath, Gastroenterol

961   Rep, 5, 193-199, 2017.

962   Hartmann, J.-M., Boulet, C., and Robert, D.: Collisional Effects on Molecular Spectra, Elsevier Science,

963   2008.

964   Henne, S., Brunner, D., Folini, D., Solberg, S., Klausen, J., and Buchmann, B.: Assessment of

965   parameters describing representativeness of air quality in-situ measurement sites, Atmos. Chem.

966   Phys., 10, 3561-3581, 2010.

967   Hodges, J. T., Layer, H. P., Miller, W. W., and Scace, G. E.: Frequency-stabilized single-mode cavity

968   ring-down apparatus for high-resolution absorption spectroscopy, 75, 849-863, 2004.

969   Keeling, R. F.: Development of an Interferometric Oxygen Analyzer for Precise Measurement of the

970   Atmospheric O_2 Mole Fraction, UMI, 1988a.

971   Keeling, R. F.: Measuring correlations between atmospheric oxygen and carbon dioxide mole

972   fractions: A preliminary study in urban air, J Atmos Chem, 7, 153-176, 1988b.

973   Keeling, R. F. and Manning, A. C.: 5.15 - Studies of Recent Changes in Atmospheric O2 Content A2 -

974   Holland, Heinrich D. In: Treatise on Geochemistry (Second Edition), Turekian, K. K. (Ed.), Elsevier,

975   Oxford, 2014.

976   Keeling, R. F. and Shertz, S. R.: Seasonal and Interannual Variations in Atmospheric Oxygen and

977   Implications for the Global Carbon-Cycle, Nature, 358, 723-727, 1992.

978   Keeling, R. F., Stephens, B. B., Najjar, R. G., Doney, S. C., Archer, D., and Heimann, M.: Seasonal

979   variations in the atmospheric O-2/N-2 ratio in relation to the kinetics of air-sea gas exchange, Global

980   Biogeochem Cy, 12, 141-163, 1998.

981   Lamouroux, J., Sironneau, V., Hodges, J. T., and Hartmann, J. M.: Isolated line shapes of molecular

982   oxygen: Requantized classical molecular dynamics calculations versus measurements, Physical

983   Review A, 89, 042504, 2014.

984   Le Quéré, C., Andrew, R. M., Friedlingstein, P., Sitch, S., Pongratz, J., Manning, A. C., Korsbakken, J. I.,

985   Peters, G. P., Canadell, J. G., Jackson, R. B., Boden, T. A., Tans, P. P., Andrews, O. D., Arora, V. K.,

986   Bakker, D. C. E., Barbero, L., Becker, M., Betts, R. A., Bopp, L., Chevallier, F., Chini, L. P., Ciais, P.,

987   Cosca, C. E., Cross, J., Currie, K., Gasser, T., Harris, I., Hauck, J., Haverd, V., Houghton, R. A., Hunt, C.

988   W., Hurtt, G., Ilyina, T., Jain, A. K., Kato, E., Kautz, M., Keeling, R. F., Klein Goldewijk, K., Körtzinger, A.,

989   Landschützer, P., Lefèvre, N., Lenton, A., Lienert, S., Lima, I., Lombardozzi, D., Metzl, N., Millero, F.,

990   Monteiro, P. M. S., Munro, D. R., Nabel, J. E. M. S., Nakaoka, S. I., Nojiri, Y., Padín, X. A., Peregon, A.,

991   Pfeil, B., Pierrot, D., Poulter, B., Rehder, G., Reimer, J., Rödenbeck, C., Schwinger, J., Séférian, R.,

992   Skjelvan, I., Stocker, B. D., Tian, H., Tilbrook, B., van der Laan-Luijkx, I. T., van der Werf, G. R., van

993   Heuven, S., Viovy, N., Vuichard, N., Walker, A. P., Watson, A. J., Wiltshire, A. J., Zaehle, S., and Zhu,

994   D.: Global Carbon Budget 2017, Earth Syst. Sci. Data Discuss., 2017, 1-79, 2017.

995   Manning, A.: Temporal variability of atmospheric oxygen from both continuos and measurements

996   and a flask sampling network: tools for studying the global carbon cycle, Ph.D. Ph.D., University of

997   California, San Diego, San Diego, Calofornia, USA, 2001.

998 Manning, A. C. and Keeling, R. F.: Global oceanic and land biotic carbon sinks from the Scripps

999 atmospheric oxygen flask sampling network, Tellus B, 58, 95-116, 2006.

1000 Manning, A. C., Keeling, R. F., and Severinghaus, J. P.: Precise atmospheric oxygen measurements

1001 with a paramagnetic oxygen analyzer, Global Biogeochem Cy, 13, 1107-1115, 1999.

1002 Marrero, T. R. and Mason, E. A.: Gaseous Diffusion Coefficients, Journal of Physical and Chemical

1003 Reference Data 1, 3, 1972.

1004 Martin, N. A., Ferracci, V., Cassidy, N., and Hoffnagle, J. A. J. A. P. B.: The application of a cavity ring-

1005 down spectrometer to measurements of ambient ammonia using traceable primary standard gas

1006 mixtures, 122, 219, 2016.

1007 Mckay, L. F., Eastwood, M. A., and Brydon, W. G.: Methane Excretion in Man - a Study of Breath,

1008 Flatus, and Feces, Gut, 26, 69-74, 1985.

1009 Nevison, C. D., Keeling, R. F., Kahru, M., Manizza, M., Mitchell, B. G., and Cassar, N.: Estimating net

1010 community production in the Southern Ocean based on atmospheric potential oxygen and satellite

1011 ocean color data, Global Biogeochem Cy, 26, 2012.

1012 Oney, B., Henne, S., Gruber, N., Leuenberger, M., Bamberger, I., Eugster, W., and Brunner, D.: The

1013 CarboCount CH sites: characterization of a dense greenhouse gas observation network, Atmos.

1014 Chem. Phys., 15, 11147-11164, 2015.

1015 Press, W. H., Teukolsky, S. A., Vetterling, W. T., and Flannery, B. P.: Numerical Recipes 3rd Edition:

1016 The Art of Scientific Computing, Cambridge Printing Press, Cambridge, England, 1986.

1017 Press, W. H., Teukolsky, S. A., Vetterling, W. T., and Flannery, B. P.: Numerical recipes in C: the art of

1018 scientific computing, Cambridge University Press, London, 1992.

1019 Ryter, S. W. and Choi, A. M. K.: Carbon monoxide in exhaled breath testing and therapeutics, J Breath

1020 Res, 7, 2013.

1021 Satar, E., Berhanu, T. A., Brunner, D., Henne, S., and Leuenberger, M.: Continuous CO2/CH4/CO

1022 measurements (2012–2014) at Beromünster tall tower station in Switzerland, Biogeosciences, 13,

1023 2623-2635, 2016.

1024 Schibig, M. F., Steinbacher, M., Buchmann, B., van der Laan-Luijkx, I. T., van der Laan, S., Ranjan, S.

1025 and Leuenberger, M. C,: Comparison of continuous in situ CO2 observations at Jungfraujoch using

1026 two different measurement techniques, Atmospheric Measurement Techniques

1027 , 8, 57-68, 10.5194/amt-8-57-2015, 2015.

1028 Severinghaus, J. P.: Studies of the terresterial O2 and carbon cycles in sand dune gases and in

1029 Biosphere Doctoral Ph.D., Columbia University, New York, USA, 1995.

1030 Steig, E. J., Gkinis, V., Schauer, A. J., Schoenemann, S. W., Samek, K., Hoffnagle, J., Dennis, K. J., and

1031 Tan, S. M.: Calibrated high-precision [17]O-excess measurements using cavity ring-down

1032 spectroscopy with laser-current-tuned cavity resonance, Atmos. Meas. Tech., 7, 2014.

1033 Stephens, B. B., Bakwin, P. S., Tans, P. P., Teclaw, R. M., and Baumann, D. D.: Application of a

1034 differential fuel-cell analyzer for measuring atmospheric oxygen variations, J Atmos Ocean Tech, 24,

1035 82-94, 2007.

1036 Sturm, P., M. Leuenberger, F.L. Valentino, B. Lehmann, and B. Ihly, Measurements of CO_2, its stable

1037 isotopes, O_2/N_2, and ^{222}Rn at Bern, Switzerland, *Atmospheric Chemistry and Physics*, *6*, 1991-2004,

1038 2006.

1039 Tennyson, J., Bernath, P. F., Campargue, A., Császár, A. G., Daumont, L., Gamache, R. R., Hodges, J. T.,

1040 Lisak, D., Naumenko, O. V., Rothman, L. S., Tran, H., Zobov, N. F., Buldyreva, J., Boone, C. D., De Vizia,

1041 M. D., Gianfrani, L., Hartmann, J.-M., McPheat, R., Weidmann, D., Murray, J., Ngo, N. H., and

1042 Polyansky, O. L.: Recommended isolated-line profile for representing high-resolution spectroscopic

1043 transitions (IUPAC Technical Report), 86, 1931–1943, 2014.

1044   Tohjima, Y.: Method for measuring changes in the atmospheric O-2/N-2 ratio by a gas

1045   chromatograph equipped with a thermal conductivity detector, J Geophys Res-Atmos, 105, 14575-

1046   14584, 2000.

1047   Tran, H., Turbet, M., Hanoufa, S., Landsheere, X., Chelin, P., Ma, Q., Hartmann, J.: The CO_2–

1048   broadened H_2O continuum in the 100–1500 cm-1 region: Measurements, predictions and empirical

1049   model, Journal of Quantitative Spectroscopy and Radiative Transfer, 230, 75-80, 2019.

1050   Valentino, F. L., Leuenberger, M., Uglietti, C., and Sturm, P.: Measurements and trend analysis of O_2,

1051 CO_2 and $\delta 13C$ of CO_2 from the high altitude research station Junfgraujoch, Switzerland — A

1052   comparison with the observations from the remote site Puy de Dôme, France, Sci Total Environ, 391,

1053   203-210, 2008.

1054   Varghese, P. L. and Hanson, R. K.: Collisional narrowing effects on spectral line shapes measured at

1055   high resolution, Appl. Opt., 23, 2376-2385, 1984.

1056   Wójtewicz, S., Cygan, A., Masłowski, P., Domysławska, J., Wcisło, P., Zaborowski, M., Lisak, D.,

1057   Trawiński, R. S., and Ciuryło, R.: Spectral line-shapes of oxygen B-band transitions measured with

1058   cavity ring-down spectroscopy, Journal of Physics: Conference Series, 548, 012028, 2014.

1059   Wolf, P. G., Parthasarathy, G., Chen, J., O'Connor, H. M., Chia, N., Bharucha, A. E., and Gaskins, H. R.:

1060   Assessing the colonic microbiome, hydrogenogenic and hydrogenotrophic genes, transit and breath

1061   methane in constipation, Neurogastroent Motil, 29, 2017.

1062   Zellweger, C., Forrer, J., Hofer, P., Nyeki, S., Schwarzenbach, B., Weingartner, E., Ammann, M., and

1063   Baltensperger, U.: Partitioning of reactive nitrogen (NO_y) and dependence on

1064   meteorological conditions in the lower free troposphere, Atmos. Chem. Phys., 3, 779-796, 2003.

1065